THE GEOLOGICAL SOCIETY OF AMERICA®

Extensive Early Cretaceous arc-like magmatic rocks in central Tibet manifest subduction rollback of the Neo-Tethyan ocean

Ding-Jun Wen[1,2], Xiumian Hu[2,†], Reiner Klemd[3], Xiao-Lei Wang[2], Rongfeng Ge[2], An-Lin Ma[2], Timothy Chapman[4], Wei-Wei Xue[5], and Yi-Wei Xu[6]

[1]*School of Earth Sciences, East China University of Technology, Nanchang 330013, China*
[2]*State Key Laboratory of Mineral Deposits Research, School of Earth Sciences and Engineering, Nanjing University, Nanjing 210023, China*
[3]*GeoZentrum Nordbayern, Friedrich-Alexander Universität Erlangen-Nürnberg, Schlossgarten 5, 91054 Erlangen, Germany*
[4]*Earth Science, School of Environmental and Rural Science, University of New England, Armidale 2351, New South Wales, Australia*
[5]*State Key Laboratory of Isotope Geochemistry, Guangzhou Institute of Geochemistry, Chinese Academy of Sciences, Guangzhou 510640, China*
[6]*Nanjing Institute of Geology and Palaeontology, Chinese Academy of Sciences, Nanjing 210008, China*

ABSTRACT

Spatiotemporal distribution of magmatism in continental arcs is generally accompanied by compositional change of igneous rocks. However, it remains unclear whether and how the variation footprint and geochemical affinities of magmatism in fossil magmatic arcs are effective for reconstructing subduction polarity. In this study, new geochronological, mineralogical, geochemical, and Sr-Nd-Hf isotope data are presented to characterize the Early Cretaceous (ca. 130–110 Ma) bimodal volcanic rocks of the Zenong Group in central Lhasa, central Tibet. Our data show that the Zenong Group volcanic rocks are dominated by rhyolite and dacite, subordinate basalt, and local andesite. The basalts have enriched Sr-Nd-Hf isotopic compositions and arc-like trace elements, suggesting a lithospheric mantle source in the spinel stability field with minor asthenospheric mantle contributions. The andesites have similar Mg# values and isotopic compositions, indicating a fractionation origin from the basaltic magmas. The coeval dacites and rhyolites display relatively low Mg# values and variable isotopic compositions, pointing to an ancient lower crust source with minor mantle contribution. The bimodal compositional characteristics and contrasting magma sources of the volcanic rocks indicate an extensional setting. We propose that the northward migration of the Early Cretaceous (ca. 130–110 Ma) magmatism in central Lhasa is the result of backarc rifting associated with slab rollback of the subducting Neo-Tethyan oceanic plate. The backarc rifting model helps to reconcile ca. 130–110 Ma sedimentary-magmatic evolution records in a broader region, including the Xigaze forearc spreading, magmatic lull in the Gangdese arc, and volcanic–sedimentary rocks in the central Lhasa subterrane.

INTRODUCTION

The spatiotemporal variation of arc magmatism is controlled by many processes such as trench retreat versus advance, flat slab or rollback subduction, frontal arc migration, and changes in the upper plate deformation over time (DeCelles et al., 2009; Sharples et al., 2014). However, quantifying the relationship of the slab geometry and kinematics to the tectonics poses a major challenge due to the commonly incomplete preservation of deformational and structural records. In this regard, magmatic arcs in fossil orogens are useful for geometry and kinematic reconstructions (e.g., Collins et al., 2011; Guo et al., 2021) because slab movement–related deep dynamic processes may cause melting of diverse crustal and mantle sources, generating a wide range of magmatic rocks with distinct mineral assemblages and whole-rock compositions. As the surface expression of crust-mantle processes in depth, volcanic arcs record intrinsic information about the generation and evolution of large silicic magmatic systems (Forni et al., 2018), such as rates and time scales of magmatic processes and involved potential sources and geodynamic settings (Bustamante et al., 2016; Chapman et al., 2017; Castro et al., 2021).

The geological evolution of the central Lhasa subterrane between ca. 130 Ma and 110 Ma is characterized by the deposition of a series of thick carbonate and siliciclastic rocks in a shelf-coastal and fluvial environment (Sun et al., 2017; Xu et al., 2022), and the voluminous eruption of volcaniclastic and volcanic rocks in a continental environment located hundreds of kilometers inland from the coast (Zhu et al., 2011; Chen et al., 2014; Chapman and Kapp, 2017; Li et al., 2023). This extensive sedimentary-magmatic evolution records the gradual change of the sedimentary environment from the marine to the continental facies (Sun et al., 2017; Lai et al., 2019a, 2019b), as well as the oceanward-directed magmatism migration (Li et al., 2023) in the central and northern Lhasa subterranes. Furthermore, this sedimentary-magmatic episode occurred simultaneously with the magmatic lull in the southern Lhasa subterrane and the forearc extension in the Xigaze forearc basin (Ji et al., 2009; Wang et al., 2017). Nevertheless, despite its widespread impact on the tectonic development of the Lhasa terrane, the exact mechanisms that initiated this major sedimentary-magmatic episode remain controversial.

One hypothesis to explain the flip in tectonic regime involves the transition to low-angle or flat-slab subduction during the Early Cretaceous (Kapp et al., 2003; Kapp and DeCelles, 2019; Leier et al., 2007; Zhang et al., 2004; Chapman et al., 2018). Alternatively, magmatic flare-ups in central Tibet have been proposed to be a result of the southward subduction of the Bangong-

Xiumian Hu https://orcid.org/0000-0002-5401-8682
[†]huxm@nju.edu.cn

GSA Bulletin;
Published online 7 April 2025

https://doi.org/10.1130/B38080.1.

Nujiang Tethys Ocean based on their arc-like geochemical signatures (Zhu et al., 2009; Chen et al., 2014; Li et al., 2018). Crucial points of these two models are conflicting and present distinct alternatives for the petrogenesis of the relevant volcanism as well as coeval plutonic rocks (Li et al., 2023; Wang et al., 2023; Yu et al., 2024). To help resolve these possibilities, we examined and analyzed volcanic rocks from the central Lhasa subterrane. Bimodal distinctions in the volcanic rock compositions provide clarity on possible tectonic regimes.

GEOLOGICAL BACKGROUND AND SAMPLING

The Himalayan-Tibetan plateau is a typical continent-continent collisional zone, which is interpreted to have formed by the northward accretion of several roughly east-west–trending terranes, including the Songpan–Ganze, Qiangtang, and Lhasa, and the Tethyan Himalaya from north to south (Fig. 1A; Yin and Harrison, 2000). The Lhasa terrane is sandwiched between the Himalayan belt to the south and the Qiangtang terrane to the north, bounded by the Bangong–Nujiang and Indus–Yarlung Zangbo suture zones, respectively (Fig. 1A; Yin and Harrison, 2000; Zhu et al., 2011). Based on the differences of the basement rocks and the sedimentary cover, the Lhasa terrane has been subdivided into the northern, central, and southern Lhasa subterranes that are roughly separated by the Shiquan River–Nam Tso Mélange Zone to the north and the Luobadui–Milashan fault to the south of central Lhasa (Fig. 1A; Zhu et al., 2009). The northern Lhasa subterrane is mainly composed of Triassic–Cretaceous sedimentary rocks and extensive Early Cretaceous volcanic rocks and associated coeval intrusive rocks (Zhu et al., 2011). The central Lhasa subterrane is a microcontinent with Archean to Proterozoic basement rocks, overlain by Carboniferous–Permian metasedimentary and Late Jurassic–Early Cretaceous volcano-sedimentary sequences (Kapp et al., 2005; Leier et al., 2007; Zhu et al., 2011, 2013), and minor Late Jurassic to Early Cretaceous granitoids. Spatially extensive arc-like magmatic rocks occur in the north of the central Lhasa subterrane (Zhu et al., 2011, 2013). The southern Lhasa subterrane is characterized by the Gangdese batholith and Early Jurassic–Cenozoic volcanic successions (Fig. 1B; Mo et al., 2008; Ji et al., 2009; Ma et al., 2021; Wen et al., 2023; Zhu et al., 2023), the latter of which consists of the Early Jurassic Yeba Formation, the Sangri Group, and the Cenozoic Linzizong volcanic succession (Zhu et al., 2013).

The volcanic rocks investigated here belong to the Zenong Group in central Lhasa (Fig. 1B). Available studies mainly focus on the relationship between the petrogenesis and the geodynamic processes, revealing only limited information on the field relationships. Stratigraphic section measurements indicate that the Zenong Group unconformably overlies the Paleozoic strata and mainly consists of basaltic to rhyolitic lavas, volcaniclastic rocks, and sedimentary rocks (carbonate and siliciclastic rocks; Figs. 2A–2F; Coulon et al., 1986; Pan, 2006). Thirty-eight relatively fresh volcanic rock samples were collected in the central and eastern parts of the Zenong Group (Fig. 1), including 17 basaltic, 10 andesitic, three dacitic, and eight rhyolitic samples. The basalts mainly display an intergranular texture with phenocrysts of plagioclase (5%–10%) and minor clinopyroxene (<10%) in an intergranular groundmass of fine-grained plagioclase, pyroxene, magnetite, and glass (Figs. 2C and 2G). The andesites are porphyritic with phenocrysts of plagioclase and minor clinopyroxene (Figs. 2D and 2H). The dacites and rhyolites are dominated by plagioclase (25%–30%) and quartz (15%) phenocrysts, while the groundmass mainly consists of microlitic felsic minerals (Figs. 2I–2J). Minor secondary alteration occurs in most rock types and mainly includes epidote and calcite, replacing the plagioclase (Figs. 2H and 2I).

The Zenong Group is dominated by the presence of mafic–silicic volcanic rocks and volcaniclastic rocks, interbedded within bimodal volcanic eruptive cycles (Fig. 3). For instance, the rhyolite-dacite-volcaniclastic rocks and basalt assemblages record three felsic to mafic eruptive cycles in the Deqing section and one in the

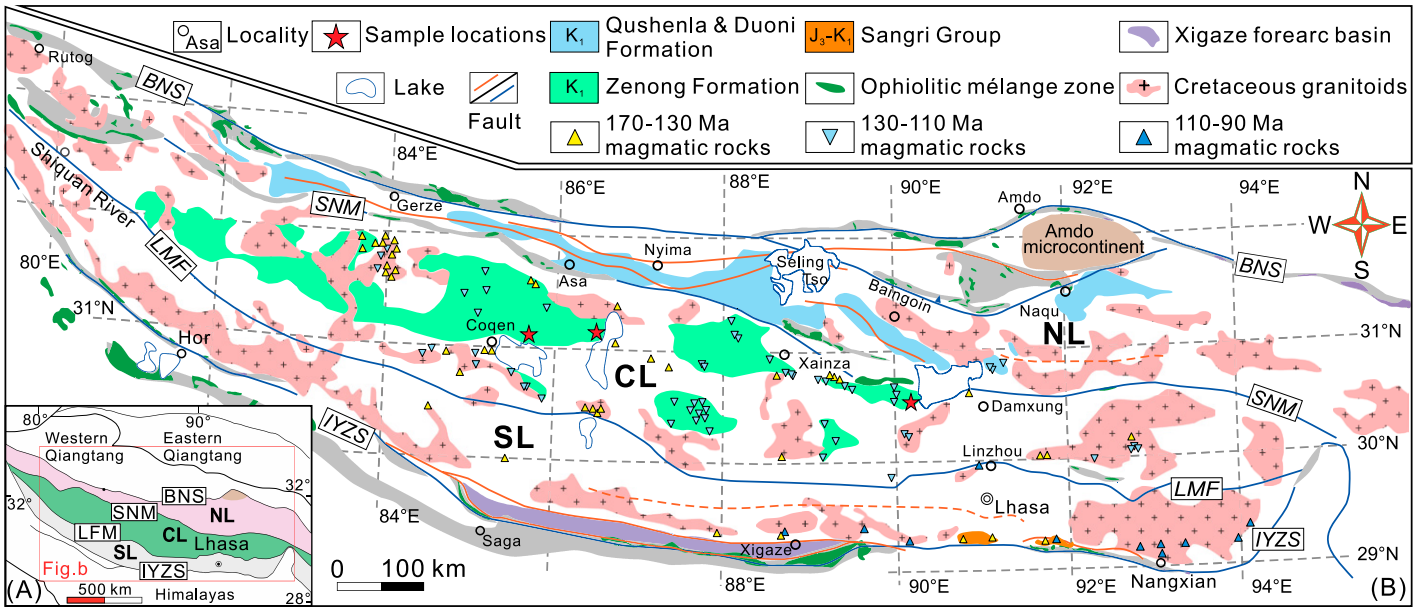

Figure 1. (A) Tectonic subdivisions of the Tibetan Plateau (Zhu et al., 2013), showing the main suture zones between the major terranes: BNS—Bangong-Nujiang suture; IYZS—Indus-Yarlung-Zangpo suture; SNM—Shiquan River-Nam Tso suture. (B) Simplified geological map showing the time-space distributions of the Late Jurassic–Early Cretaceous igneous rocks in the Lhasa Terrane. CL—central Lhasa; NL—northern Lhasa; SL—southern Lhasa; LMF—Luobadui–Milashan fault. See Table S8 for the data source (see text footnote 1).

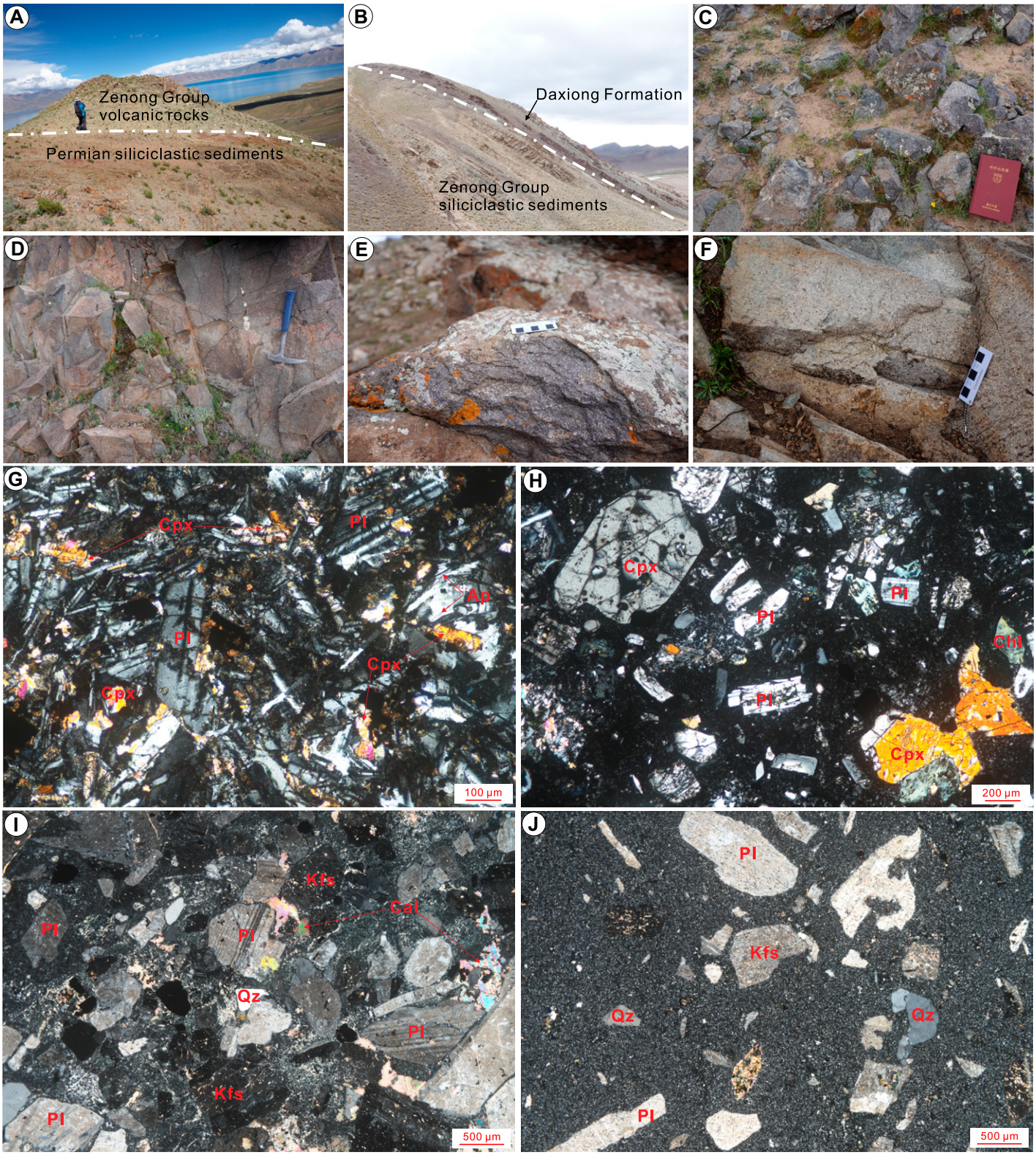

Figure 2. Representative photos of geological field observations and petrography (plane-polarized light) of the Zenong Group volcanic rocks: (A–B) stratigraphic contact between the Zenong Group and Paleozoic Laga Formation and Late Cretaceous Daxiong Formation; (C–F) field outcrop of basalt, andesite, dacite, and rhyolite; (G–J) photomicrographs of representative basalt, andesite, dacite, and rhyolite. Ap—apatite; Cal—calcite; Chl—chlorite; Cpx—clinopyroxene; Kfs—K-feldspar; Pl—plagioclase; Qz—quartz.

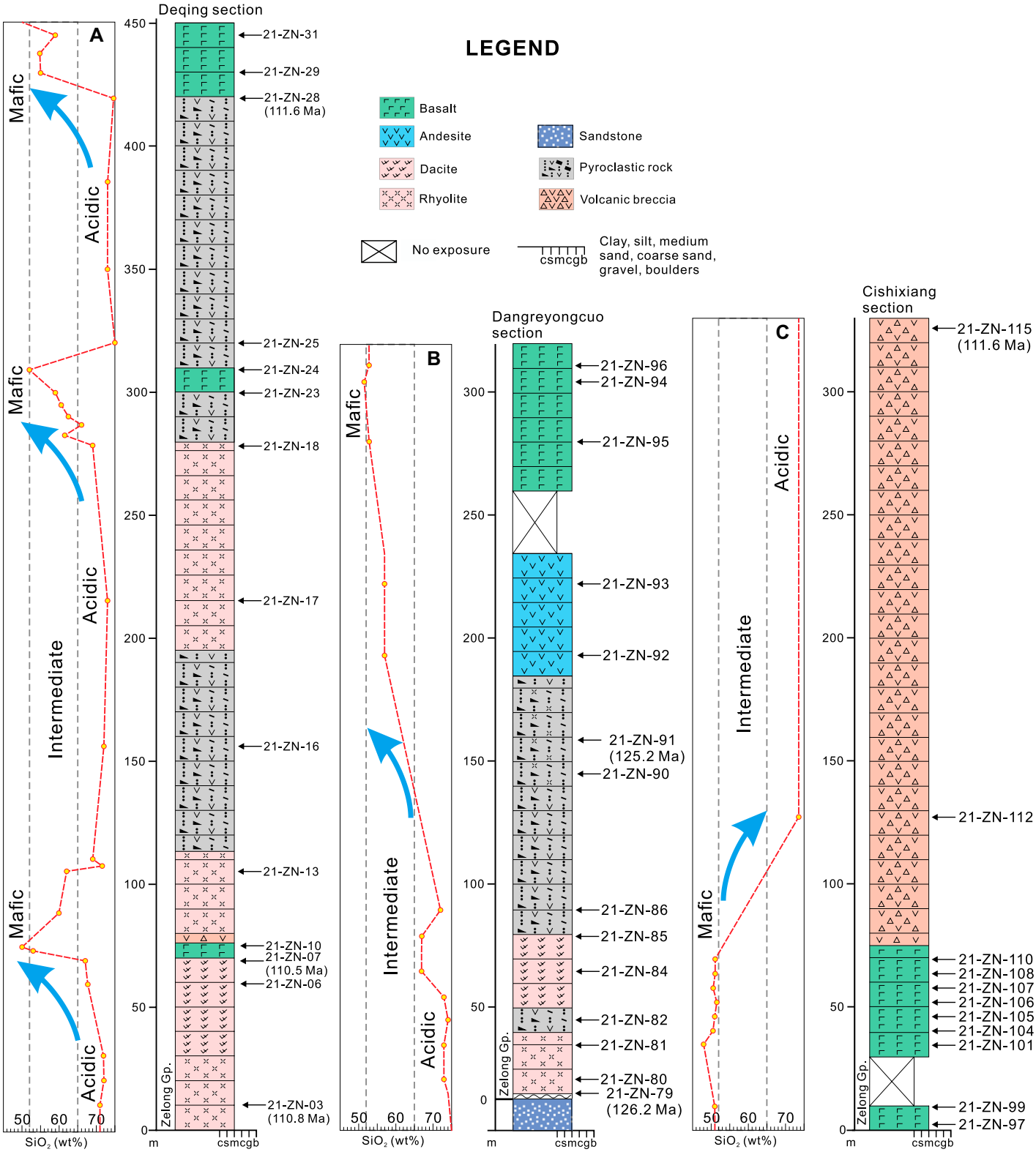

Figure 3. Compositional and lithologic variations of the representative Zenong Group volcanic–volcaniclastic rock sections: (A) Deqing section, (B) Dangreyong Tso section, and (C) Cishixiang section.

Dangreyongcuo section (Figs. 3A and 3B). In comparison, the Cishixiang bimodal volcanic suite mainly comprises basalt and felsic volcanic breccias (Fig. 3C). The compositional bimodality and evolution of the Zenong Group volcanic rocks are revealed by field survey profiles and whole-rock major elements analysis, as shown by three stratigraphic columns (Fig. 3).

ANALYTICAL METHODS

Zircon U–Pb Age Dating and Trace Element Analyses

Zircon laser ablation–inductively coupled plasma–mass spectrometry (LA-ICPMS) U–Pb dating was carried out at State Key Laboratory for Mineral Deposits Research, School of Earth Sciences and Engineering, Nanjing University (MiDeR-NJU), Nanjing, China, utilizing a system consisting of ASI RESOlution S-155 193 nm ArF Excimer laser coupled to Thermo Scientific iCAP Qc quadrupole ICP-MS.

U–Pb age data were collected by ablating with laser beam diameters of 29 μm, a beam energy density of ~3.5 J/cm^2, and a repetition rate of 5 Hz. Each analysis includes 20 s of background, 50 s ablation, and 20 s of washout. With an ablation rate of ~0.1 μm/pulse, 50 s ablation at the smallest beam diameter will produce an ablation crater with a diameter/depth ratio of <1. A fully analytical session typically consists of several blocks of eight standard analyses (two zircon standard 91500, two zircons standard Plešovice, one NIST610 standard glass, one NIST612 standard glass) followed by eight unknown samples. The $^{207}Pb/^{206}Pb$, $^{206}Pb/^{238}U$, $^{207}U/^{235}U$ ($^{235}U = {}^{238}U/137.88$), and $^{208}Pb/^{232}Th$ ratios were corrected by using zircon standard 91500 as an external standard (isotope dilution–thermal ionization mass spectrometry $^{206}Pb/^{238}U$ age data at 1062.4 ± 0.8 Ma; Wiedenbeck et al., 1995). Data reduction was performed using ICPMS-DataCal version 9.9 (Liu et al., 2008), and Isoplot version 4.15 (Ludwig, 2012) was used to make concordia plots and calculate weighted averages.

Zircon Hf Isotopes

Hafnium isotopic ratios of zircon were conducted in situ using a Nu Plasma II multicollector (MC)-ICP-MS (Wrexham, UK) in combination with an ASI RESOlution S-155 193 nm ArF excimer ablation system (Canberra, Australia) at the Nanjing FocuMS Technology Co. Ltd. The 193 nm ArF excimer laser, homogenized by a set of beam delivery systems, was focused on a zircon surface with a fluence of 4.5J/cm^2. Each acquisition incorporated a 20 s background (gas blank), followed by a spot diameter of 50 μm at a 9 Hz repetition rate for 40 s. Helium (370 ml/min) was applied as a carrier gas to efficiently transport aerosol out of the ablation cell and was mixed with argon (~0.97 L/min) via a T-connector before entering the ICP torch. The integration time of the Nu Plasma II was set to 0.3 s (equating to 133 cycles during the 40 s). Standard zircons (including GJ-1, 91500, Plešovice, Mud Tank, and Penglai) were treated as quality control for every 15 unknown samples.

Whole-Rock Major and Trace Elements

Major element whole-rock analyses were conducted using an X-ray fluorescence spectrometer (Primus II, Rigaku, Japan) at the Wuhan Sample Solution Analytical Technology Co., Ltd., Wuhan, China. The detailed procedure of sample digestion for the major element analyses is described by Zong et al. (2017). Trace element whole-rock analyses were carried out at the Nanjing FocuMS Technology Co. Ltd., Nanjing, China. About 40 mg of powder was mixed with 0.5 mL HNO_3 and 1.0 mL HF in high-pressure PTFE (polytetrafluoroethylene) bombs. These bombs were steel-jacketed and placed in the oven at 195 °C for 48 h for mafic samples and 72 h for felsic samples. Rock digestion diluent was nebulized into Agilent Technologies 7700x quadrupole ICP-MS (Hachioji, Tokyo, Japan) to determine the trace element abundances. The deviation was better than ±10% for elements exceeding 10 ppm and better than ±5% for elements exceeding 50 ppm.

Whole-Rock Sr-Nd Isotope Analysis

Isotopic compositions of Sr−Nd were measured at the Nanjing Hongchuang Geological Exploration Technology Service Co., Ltd, Nanjing, China, using a Nu Plasma II MC-ICP-MS. The Sr and Nd were extracted from natural rock samples using the procedure described by Weis et al. (2006). For each sample, the powder was weighed in high-pressure Teflon capsules with 0.5 ml 60 wt% HNO_3 and 1.0 ml 40 wt% HF, and then dissolved at 190 °C for 120 h. Afterward, samples were taken to dryness on a hotplate and reconstituted in 1.5 ml of 0.2 N HBr + 0.5 $NHNO_3$ prior to redissolution for ion exchange purification of Sr and Nd. A standard cation exchange column of Bio-Rad AG50W-X8 resin was used to separate Sr and rare earth element (REE), and high field strength elements (HFSE). Neodymium was separated from the other REE on a column using LN-specific HDEHP-coated Teflon powder as the ion exchange medium. Measured values for these U.S. Geological Survey reference materials, and U.S. National Institute of Standards and Technology (NIST) Standard Reference Material 981 were in good agreement and both within error of recommended reference values reported by Weis et al. (2006). Total procedural blanks were ~48 pg for Sr and ~36 pg for Nd. The $^{87}Sr/^{86}Sr$ data were normalized to a value of 0.1194 for the NBS 987 standard and the $^{143}Nd/^{144}Nd$ ratios to a value of 0.7219 for the JNdi-1 standard.

Mineral Chemistry

Mineral compositions were analyzed at the electron microprobe laboratory of the MiDeR-NJU (State Key Laboratory for Mineral Deposits Research at Nanjing University). A JEOL JXA-8230 electron microprobe analyzer was used to analyze the chemical composition of the respective minerals. The operating conditions were set to an acceleration voltage of 15 kV, a beam current of 20 nA, a beam diameter of 5 μm for pyroxenes, and 3 μm for feldspars.

Mineral In Situ Trace Element Analysis

The LA-ICP-MS (Agilent 7500a) at the MiDeR-NJU was used to analyze the trace element compositions of calcite, hornblende, and orthopyroxene. A Photon Machines Excite LA system (RESOlution S-155) was used in combination with a Thermo Fisher Scientific i-CAP-Q ICP-MS instrument. An ablation spot diameter of 43 μm was used, with a repetition rate of 4 Hz and laser energy of 4.8 J/cm^2. During the hornblende and orthopyroxene measurements, helium was used as the carrier gas. NIST standard reference materials NIST-610 and NIST-612, and U.S. Geological Survey basaltic glasses BCR-2G and GSE-1G were used as external standards, while ^{29}Si was used as an internal standard to correct for instrument drift. Off-line data processing was performed using the ICPMS DataCal program (Liu et al., 2008). The estimated precision was better than ±5% for major elements and ±10% for trace elements.

ANALYTICAL RESULTS

Zircon U–Pb Ages and Hf Isotopic Compositions

Six samples from the Zenong volcanic rocks in central Lhasa were selected for LA-ICP-MS zircon U–Pb dating, including two andesite (21-ZN-32 and 21-ZN-35), one dacite (21-ZN-07), and three rhyolite (21-ZN-03, 21-ZN-79, and 21-ZN-80) samples. The cathodoluminescence images of representative zircon grains are illustrated in Fig. S1, and the zircon U–Pb isotope

data are plotted in Fig. S2 and listed in Table S1.[1] The euhedral to subhedral zircon grains have a short to long prismatic habitus (50–200 μm in length), with length-to-width ratios from 1:1 to 3:1, and clear oscillatory zoning (Fig. S1). All analyzed spots exhibit varying thorium (35–1583 ppm), uranium (51–2266 ppm), and Th/U ratios (0.30–1.54; Table S1). These textural and compositional characteristics indicate an igneous origin (e.g., Belousova et al., 2002).

Zircon from the two andesite samples have variable Th (95.9–909 ppm) and U contents (138–1451 ppm) with high Th/U ratios (0.30–0.77). Twenty-four spot analyses on 24 zircon grains from sample 21-ZN-32 yielded a concordant age of 114.8 ± 0.7 Ma (mean square weighted deviates [MSWD] = 0.23; Fig. S2A). Twenty-one analyses on 21 zircon grains from sample 21-ZN-35 defined a concordant age of 111 ± 0.6 Ma (MSWD = 1.5), neglecting three strongly discordant ages, probably due to lead loss (Fig. S2B).

Zircon from the dacite sample 21-ZN-07 have variable Th (70.4–431 ppm) and U contents (87.1–400 ppm) with Th/U ratios of 0.66–1.52. Twenty-two analyses on 22 zircon grains revealed a concordant age of 110.5 ± 0.9 Ma (MSWD = 0.36; Fig. S2C).

Zircon from the three rhyolite samples have varying contents of U (53.3–687 ppm) and Th (35.5–806 ppm), with high Th/U ratios of 0.62–1.51. Eighteen spot analyses on zircon grains from sample 21-ZN-03 yielded a concordant age of 110.8 ± 0.9 Ma (MSWD = 0.78; Fig. S2D). Twenty-one analyses on 21 zircon grains from sample 21-ZN-79 revealed a concordant age of 126.2 ± 1.0 Ma (MSWD = 0.48), and 20 analyses on 20 zircon grains from 21-ZN-80 yielded a concordant age of 126.1 ± 1.1 Ma (MSWD = 0.32; Figs. S2E and S2F).

The zircon grains from five volcaniclastic rock samples have a similar morphology and internal texture as those intermediate-acid volcanic rocks. They exhibited variable Th and U contents of 35.2–3006 ppm and 50.7–3706 ppm, respectively, with variable Th/U mass ratios (0.42–2.56). The zircon grains from volcaniclastic rock samples yielded a weighted mean $^{206}Pb/^{238}U$ age of 125.2 ± 1 Ma to 105.0 ± 1 Ma (Figs. S2G–S2K).

The zircon Hf isotopic data are listed in the Table S2. The zircon grains from the two andesite samples have enriched Hf isotopic compositions, with initial $^{176}Hf/^{177}Hf$ ratios of 0.282294–0.282506, corresponding to $\varepsilon_{Hf}(t)$ values of −14.4 to −7.0 (mean = −9.7). The zircon grains from the dacite and rhyolite samples also generally show enriched Hf isotopic compositions but higher initial $^{176}Hf/^{177}Hf$ ratios of 0.282288–0.282722, corresponding to $\varepsilon_{Hf}(t)$ values of −14.4 to +0.7 (mean = −7.2).

Whole-Rock Major and Trace Element Geochemistry

The Zenong Group volcanic rocks have a varying high loss on ignition (LOI; 0.61–5.00 wt%), and the variable amounts of secondary minerals (such as calcite, epidote, and chlorite) indicate varying degrees of post-magmatic alteration, during which some mobile trace elements could have been modified. In the present study, we use Zr as an alteration-independent index element, since Zr is one of the most immobile elements during low-grade metamorphic and hydrothermal alteration processes (cf. Gibson et al., 1982). Thus, the possible mobility of elements during post-magmatic processes can be revealed—apart from a high LOI—by correlations or the lack of correlations of Zr with other elements (Polat and Hofmann, 2003). For the Zenong Group volcanic rocks with high LOI (>5 wt%), the alkali metals (such as Rb and K) and the alkaline earth metals (such as Ca, Sr, and Ba) show no correlations with Zr (Figs. S3A and S3B), thereby suggesting that their original concentrations may have been modified during post-magmatic processes (Polat and Hofmann, 2003). In contrast, the HFSE including Nb, Ta, and Hf (Figs. S3C and S3D), Y, and the REE (Figs. S3C–S3G) strongly correlate with Zr, indicating that these elements were essentially immobile during post-magmatic alteration (Polat et al., 2002). On primitive-mantle–normalized trace-element and chondrite-normalized REE diagrams, the Zenong Group volcanic rocks generally exhibit subparallel patterns of REE and HFSE concentrations (Fig. 4), which is consistent with limited mobility of the REE and HFSE as well as Th and Ti in these samples during alteration (Bienvenu et al., 1990; Staudigel et al., 1996). Therefore, these elements were used to investigate the petrogenesis of their host rocks. However, samples with very high LOI (>5.0 wt%) and pervasive alteration overprints were not considered further for the geochemical interpretation. Whole-rock major and trace element analyses are listed in Table S3 and plotted in Figure 4.

The samples show a wide range of SiO_2 with contents ranging from 47.7 wt% to 75.6 wt%, with a characteristic bimodal pattern (Fig. 4A). Most of the volcanic rock samples fall in the sub-alkaline field, with a few basalt and andesite samples plotting in the transition field between the alkaline and sub-alkaline series on the total alkalis versus silica (TAS) diagram (Fig. 4A). The basalt and andesite samples have higher Mg# (55–39) than the coeval dacite and rhyolite samples (Mg# = 37–14) and plot above the field of meta-basalt partial melting at pressures between 1.5 GPa and 3.8 GPa in the Mg# versus SiO_2 diagram (Fig. 4B).

The normalized multi-element patterns (Fig. 4C) of the basalts are relatively depleted in Nb, Ta, and Ti and enriched in incompatible elements like Ba, Th, U, and Pb, exhibiting arc-like geochemical signatures. The chondrite-normalized REE patterns (Fig. 4D) of all samples are characterized by low REE abundances, flat heavy REE (HREE) pattern, minor light REE (LREE) enrichment with $(La/Sm)_N$ ratios of 2.70–3.09, and the lack of Eu anomalies, similar to modern enriched mid-ocean-ridge basalt (E-MORB). The chondrite-normalized REE patterns of the coeval andesites display a LREE enrichment with $(La/Sm)_N$ ratios of 2.24–4.26 and slightly negative Eu anomalies (Fig. 4C). Likewise, all andesite samples are characterized by HFSE (Nb, Ta, P, and Ti)–depleted and large-ion lithophile elements (LILE; e.g., Rb, Ba, Pb, and Th)–enriched normalized multi-element patterns (Fig. 4D), but have higher REE and incompatible elements when compared with the coeval basalts. In comparison with intermediate to mafic volcanic rocks, the dacite and rhyolite samples exhibit significant enrichments of REE and incompatible elements but show moderately negative Eu anomalies ($Eu/Eu^* = 0.48–0.84$) as displayed by the chondrite-normalized REE and primitive mantle-normalized multi-element patterns (Fig. 4).

Whole-Rock Sr-Nd Isotopes

Whole-rock Sr and Nd isotopic data are listed in Table S4. The initial Sr isotopic ratios and $\varepsilon_{Nd}(t)$ and $\varepsilon_{Hf}(t)$ values were calculated using the zircon U–Pb ages (t = 115 Ma).

Seven basalt samples have a wide range of initial $^{87}Sr/^{86}Sr$ ratios from 0.70734 to 0.71069 and $\varepsilon_{Nd}(t)$ values from −5.22 to +1.97. Two andesite samples exhibit variable initial $^{87}Sr/^{86}Sr$ ratios of 0.70762–0.71037 and $\varepsilon_{Nd}(t)$ values of −5.39 to −1.47. Both the dacite and rhyolite samples have relatively constant initial $^{87}Sr/^{86}Sr$ ratios of 0.70752 and 0.70745 and $\varepsilon_{Nd}(t)$ values of −2.97 and −2.80, respectively.

Mineral Chemistry

Clinopyroxene from the basalt (21-ZN-24, 21-ZN-99, and 21-ZN-155) and the andesite (21-ZN-93) are augites with a relatively homogeneous composition of $Wo_{37–42}En_{40–47}Fs_{13–20}$ and $Wo_{38–41}En_{42–48}Fs_{14–19}$, and Mg# values of

[1]Supplemental Material. Table S1–S9 and Figures S1–S6. Please visit https://doi.org/10.1130/GSAB.S.28593104 to access the supplemental material; contact editing@geosociety.org with any questions.

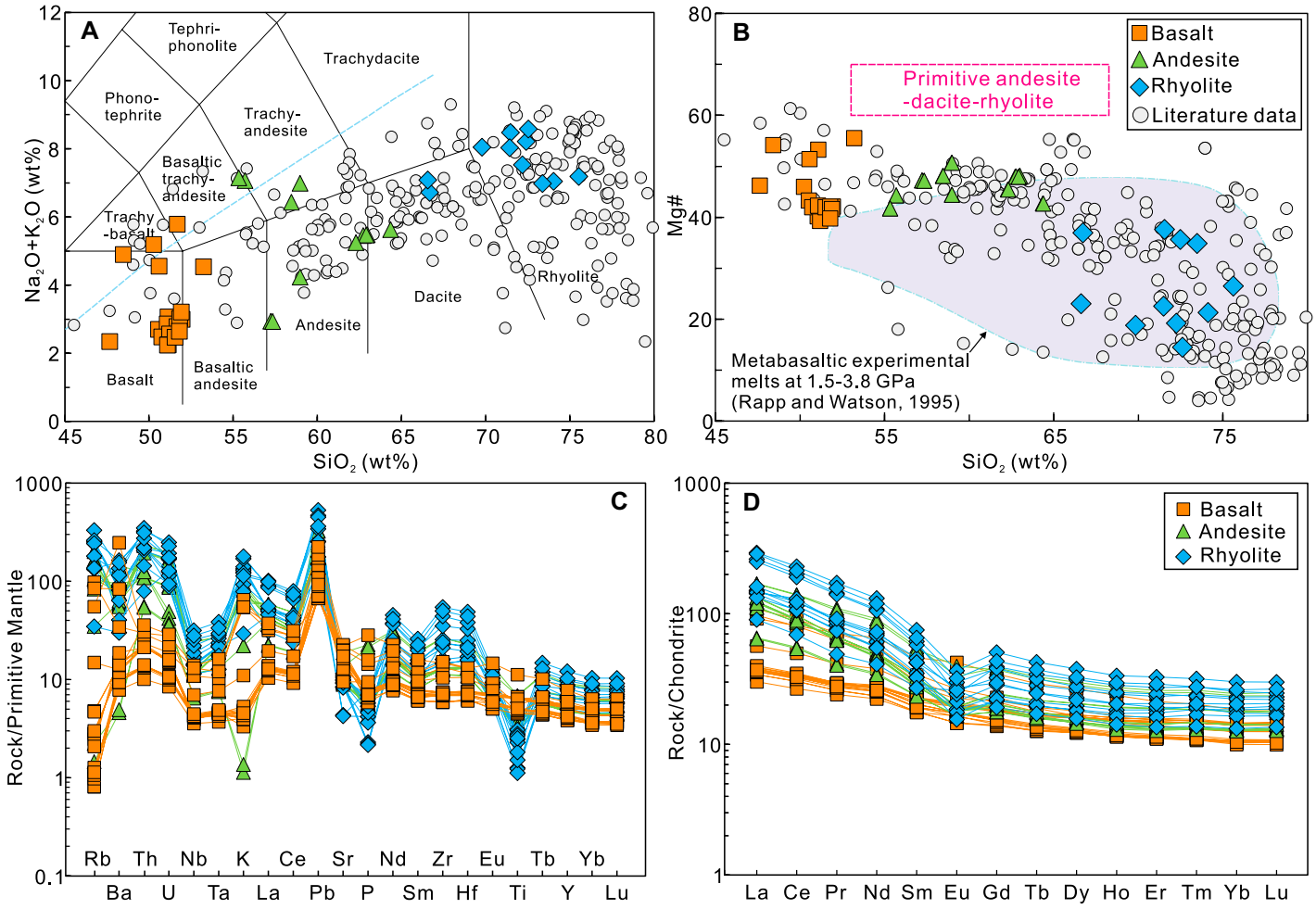

Figure 4. (A) SiO_2 vs. ($Na_2O + K_2O$) discrimination diagram (after Middlemost, 1994), and (B) SiO_2 vs. Mg# diagrams for the Zenong Group volcanic rocks. Mg# values of metabasaltic experimental melts at 1.5–3.8 GPa are from Rapp and Watson (1995). (C) Primitive mantle–normalized multielement patterns. (D) Chondrite-normalized rare earth element patterns (values for primitive mantle and chondrite are from Sun and McDonough, 1989). Literature sources of the Early Cretaceous magmatic rocks are listed in Table S8 (see text footnote 1).

0.67–0.77 and 0.69–0.77, respectively (Table S5 and Fig. 5A). Clinopyroxene in these samples exhibit Fe–Mg equilibrium conditions with the whole-rock compositions (Fig. 5A; Putirka, 2008). Plagioclase in the basalt has labradorite to bytownite composition, with $An_{54–86}$ (Table S5). All of the plagioclase grains in the basalt samples show typical core-rim textures and normal zoning and are characterized by bytownite cores and labradorite rims.

The chondrite-normalized REE patterns of the clinopyroxene from the basalts are bell-shaped, showing relative depletions in both the LREE and the HREE with respect to the middle REE (MREE; Table S6 and Fig. 5B). However, the clinopyroxenes from the andesite are about three times more enriched in LREE and five times in MREE-HREE than those from the basalts (Fig. 5B). In addition, the clinopyroxenes in the basalt are characterized by weak to insignificant negative Eu anomalies (Eu/Eu* = 0.69–1.05, calculated as Eu/Eu* = Eu_N/Squrt [Sm_N*Gd_N], normalized to CI) and high Sr (13.7–139 ppm) and Ba (0.0–63.6 ppm) concentrations, whereas clinopyroxenes from the andesite show significant Eu anomalies (Eu/Eu* = 0.48–0.63) and relative low Sr (9.67–15.2 ppm) and Ba (0.0–2.37 ppm) contents (Table S6).

DISCUSSION

Spatiotemporal Distribution of the Zenong Group Volcanic Rocks

The results of the present study, in conjunction with detailed field investigation and published geochronological and geochemical data of the Zenong Group volcanic rocks, allow us to constrain the timing and the compositional volcanic evolution. The new zircon U–Pb ages of this study indicate that the Zenong Group volcanism began to erupt at ca. 126 Ma and ceased at ca. 105 Ma. The rhyolite sample (21-ZN-79) from the bottom of the Zenong Group volcanic successions, which unconformably overlies the Permian clastic sediments (Fig. 2A), revealed an age of 126 Ma, while two pyroclastic samples (21-ZN-135 and 21-ZN-2) with a younger $^{206}Pb/^{238}U$ age of 105 Ma from the Cuoqen and Deqin areas of the Zenong Group are overlain by the Daxiong Formation (conglomerate-bearing deposits) and the Langshan Formation (limestone), respectively (Fig. 2B). Consequently, volcanism of the Zenong Group formed in the span from ca. 126 Ma to ca. 105 Ma, which is supported by the field survey data (Figs. 2A, 2B, and 3).

Late Mesozoic magmatic rocks in the Lhasa Terrane have a distinct spatial and temporal distribution. The Jurassic–Early Cretaceous (200–130 Ma) magmatism is exposed across the entire

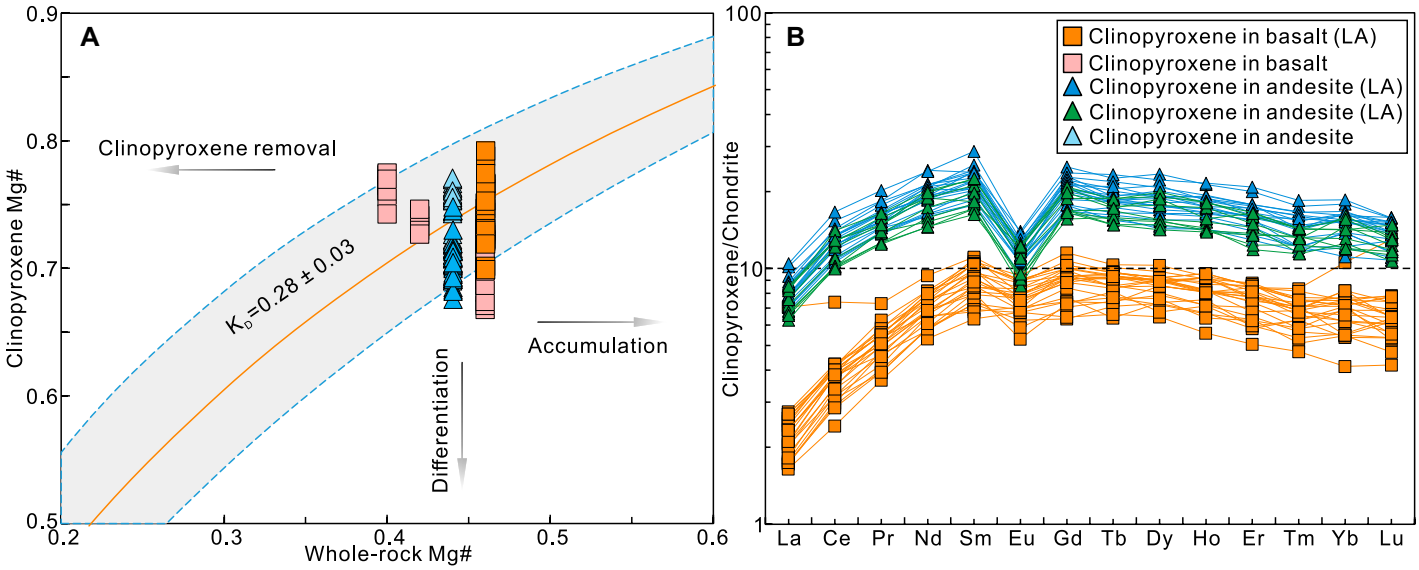

Figure 5. (A) Whole-rock Mg# vs. clinopyroxene Mg# to test the Fe–Mg exchange equilibrium. Tests employ a $D_{(Fe-Mg)} = 0.28 \pm 0.03$ for clinopyroxene (Putirka, 2008). (B) Chondrite-normalized rare earth element pattern diagrams of clinopyroxenes from the basalt and andesite. Chondrite values are taken from Sun and McDonough (1989).

Lhasa Terrane (Li et al., 2023). Comparatively, Early Cretaceous magmatic rocks (130–110 Ma), represented by the Zenong Group volcanic rocks and coeval plutons, are restricted to the central and northern Lhasa subterranes (Fig. 1). Such a distribution is indicative of northward migration of magmatism during the Early Cretaceous. Subsequent Early Cretaceous–Late Cretaceous (<110 Ma) magmatic rocks, represented by the Gangdese batholith, mostly occur in the southern Lhasa subterrane (Fig. 1). Sporadic exposures of Late Cretaceous magmatic rocks in the central and northern Lhasa subterrane are consistent with a later stage of southward migration of magmatism initiating at ca. 110 Ma. The northward and then southward migration of the late Mesozoic magmatism of the Lhasa terrane requires a switching regime of Neo-Tethyan subduction. One possibility to explain the distribution of magmatic rocks is an episode of flat subduction followed by slab roll-back. This migration pattern is consistent with those documented across the NE Asia and South China Blocks, implying a similar late Mesozoic subduction evolution (Tang et al., 2024). The adjustments in the Neo-Tethyan subduction angle should balance heat flow and mass to control the spatiotemporal footprint of magmatism (e.g., DeCelles et al., 2009; Sharples et al., 2014; Tang et al., 2024).

Petrogenesis of the Zenong Volcanic Rocks

Effects of Crustal Contamination

Mantle-derived basaltic magmas commonly undergo crustal contamination during their ascent to the surface (Wilson, 1989). However, the lack of inherited zircon in the Zenong Group volcanic rocks is indicative of minor crustal assimilation. This is consistent with the observation that the majority of samples of the Zenong Group andesites and basalts display lower initial $^{87}Sr/^{86}Sr$ ratios (0.7076–0.7107) and more negative $\varepsilon_{Nd}(t)$ values (−1.5 to −5.4) than the crustal-derived Early Cretaceous (130–110 Ma) volcanic-intrusive rocks (Fig. 6A). Moreover, the Sr–Nd–Hf isotope compositions of the volcanic rocks do not exhibit a linear correlation with increasing SiO_2 (not shown), reflecting a limited role of crustal contamination in the formation of basalts and andesites, since these elements are highly sensitive to the assimilation of crustal materials. Thorium and lanthanum are sensitive indicators of crustal contamination. The basalts have relatively low Th/La ratios (0.09–0.23), much lower than those of continental crust (Th/La = ~0.30; Plank, 2005), indicating that crustal contamination had a minor impact on the petrogenesis of these rocks. However, some of the andesite samples may have been affected by crustal contamination as suggested by their continental crust-like Th/La ratios (0.30–0.63).

Origin of the Zenong Basalt

The Zenong Group basalts are characterized by low SiO_2 and high MgO, high compatible element contents, moderate fractionation between LREE and HREE, LILE enrichment, and HFSE depletion (Table S3; Fig. 3). Low LOI values and the lack of pervasive hydrothermal overprints indicate relatively minor degrees of post-magmatic alteration. These geochemical signatures are similar to those of contemporaneous arc-like basalts for which the magmas were interpreted to have originated from an enriched mantle wedge (Chen et al., 2014). However, the Zenong basalts in this study exhibit arc-like trace element patterns and enriched isotopic compositions (Figs. 4C, 4D, and 5) with high Mg# values, implying that their mantle source was refractory, ancient, and fertile, suggesting a lithospheric mantle source (Zhu et al., 2012). The relative depletion of HFSE (e.g., Nb, Ta, and Ti) in the spider diagram is thought to be due to subduction-related metasomatism (e.g., Thirlwall et al., 1994; Duggen et al., 2005). Therefore, it is suggested that the mantle source of the Zenong basaltic rocks in the central Lhasa subterrane may have been previously modified by subduction-derived fluids/melts. The Zenong basalts show a significant enrichment of LILE and have relatively low K_2O contents, indicating a LILE-enriched mantle source (Ma et al., 2014), similar to a phlogopite- and amphibole-bearing enriched lithospheric mantle (Foley et al., 1996; Yang et al., 2007). Silicate melts in equilibrium with amphibole in the source are expected to have low Rb/Sr (<0.1) and high Ba/Rb (>20), whereas melts derived from phlogopite-bearing sources would have low Ba and Ba/Rb values (Furman and Graham, 1999; Yang et al., 2007; Ma et al., 2014). The Zenong basalts have relatively low Rb/Sr (0.01–0.13) and high Ba/Rb (3.9–129), indicating the presence of amphibole in their mantle source. Partial melts of the garnet-bearing mantle sources generally have high

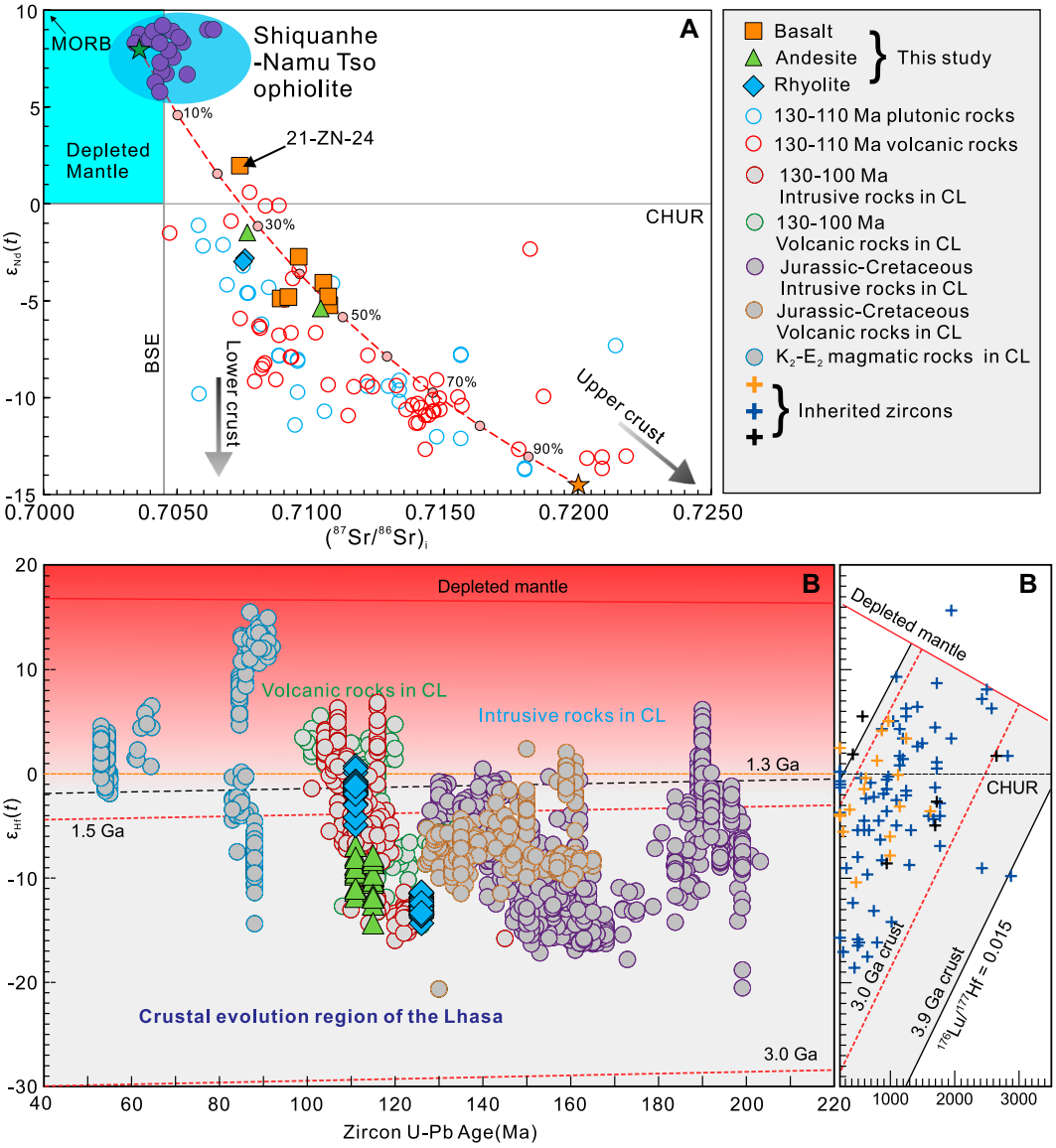

Figure 6. Isotopic plots of (A) ε_{Nd} (t = 110 Ma) vs. $(^{87}Sr/^{86}Sr)_i$ and (B) zircon $\varepsilon_{Hf}(t)$ vs. ages diagrams for the Early Cretaceous magmatic rocks in central Lhasa (CL). The data of the Shiquan River ophiolite are from Zeng et al. (2018), and of the strongly peraluminous granites (orange star) as a proxy for crustal melt are from Zhu et al. (2012). Isotopic data of Mesozoic and Cenozoic magmatic rocks from literature sources are listed in Table S8 (see text footnote 1). The isotopic data of inherited zircons are from Zhu et al. (2011). BSE—bulk silicate earth; CHUR—chondritic uniform reservoir; MORB—mid-ocean-ridge basalt.

$(Gd/Yb)_C$ ratios (>2.0), whereas melting of spinel-bearing mantle sources would produce melts with low $(Gd/Yb)_C$ ratios (<2.0; Deng et al., 2017). To help determine the melting process in the source, non-modal batch melting modeling was conducted using REE. Model parameters, partition coefficients, and all calculations are provided in Table S9. The modeling results show that the majority of the Zenong basalts have $(Gd/Yb)_C$ ratios ranging from 1.25 to 1.85, with an average value of 1.5, plotting along the partial melting curves of the spinel-bearing mantle (Fig. 7A). This implies that partial melting may have taken place in the spinel stability field (Duggen et al., 2005). In addition, the Zenong basalts have relatively low Sm/Yb (1.5–2.3) and La/Yb (4.5–13.3) ratios, plotting close to the partial melting curves of mixed mantle sources (90% enriched mantle + 10% asthenospheric mantle) with variable degrees (2%–15%) of partial melting (Fig. 7B). The inferred contribution of asthenospheric material in the mantle sources is further supported by some of the basalt samples (21-ZN-10) showing positive Nd isotopic compositions [$\varepsilon_{Nd}(t) = 2$]. We, therefore, conclude that the magmas of the Zenong Group basalts were mostly derived from low-degree partial melting of an amphibole-bearing lithospheric mantle in the spinel stability fields, with a minor input of asthenospheric mantle melt.

Origin of the Zenong Andesite

The formation mechanism of andesites remains enigmatic, and various models have been proposed, including: (1) crystallization-differentiation of mantle-derived basaltic melts (Sisson and Grove, 1993; Grove et al., 2003), (2) partial melting of the subducting slab (Kay, 1978), (3) hydrous melting of mantle wedge peridotite (Kushiro, 1975; Kelemen, 1986; Grove et al., 2003), (4) partial melting of mafic lower crust (Rapp and Watson, 1995; Lustrino, 2005), and (5) hybridization of silicic magmas and mantle-derived melts (Hildreth and Moorbath, 1988; Clemens et al., 2011).

Slab melting or slab-derived melts interacting with the mantle wedge can generate andesitic magmas (Castro, 2013), requiring the involvement of oceanic subduction. However, previously it has been suggested that the collision of the Lhasa and Qiangtang terranes occurred in the Late Jurassic, based on an integrated stratigraphic, sedimentological, and provenance study of the Jurassic stratigraphic units in the southern Qiangtang basin (Ma et al., 2017). Consequently, the central Lhasa subterrane is believed to have constituted an intra-continental block during the

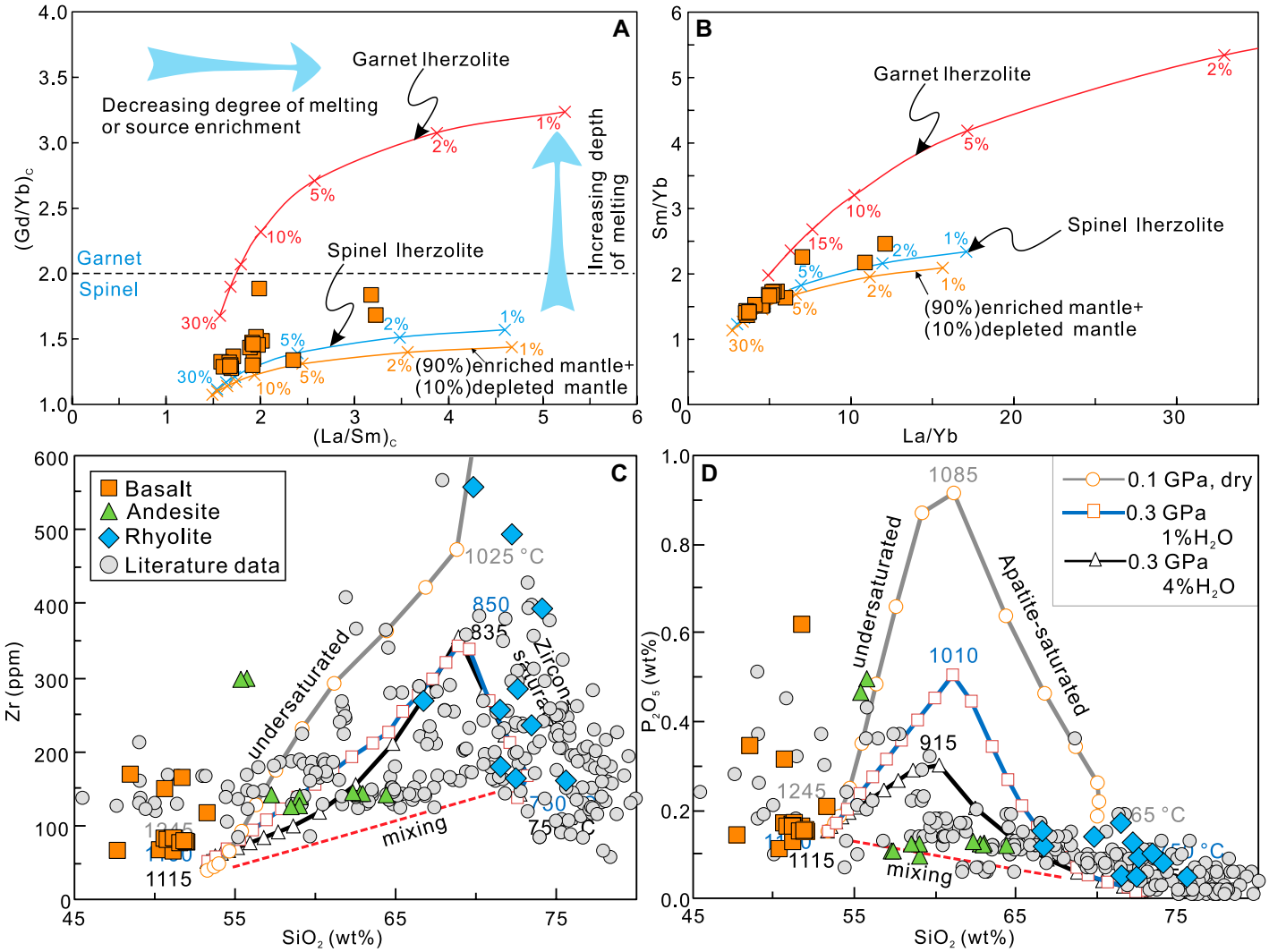

Figure 7. Plotting of (A) $(La/Sm)_C$ vs. $(Gd/Yb)_C$ and (B) La/Yb vs. Sm/Yb diagrams point to a spinel-bearing source for the Zenong Group basalts. (C–D) Zr and P_2O_5 systematics of volcanic rocks from the Zenong Group. Normalization values of the chondrite C1 after Sun and McDonough (1989). Also shown are the simulation results of non-batch melting of spinel-bearing lherzolite and garnet-bearing lherzolite with various melting degrees (parameters used in the simulation are present in Table S9; see text footnote 1).

Early Cretaceous when the Zenong andesites erupted. In addition, partial melting of the subducting slab would have produced intermediate magmas with adakite-like affinities and depleted Sr-Nd-Hf isotopic compositions, whereas the andesite samples studied here have calc-alkaline affinities and enriched Sr-Nd-Hf isotopic compositions ($\varepsilon_{Nd}(t) = -7.26$ to -4.81).

Experimental studies indicate that partial melting of the mafic lower crust would generate low Mg# (<40) melts, regardless of the degree of melting at melting pressures between 1.0 and 4.0 GPa (Rapp et al., 1999). The Zenong Group andesites have higher Mg# values (40−51) than pure crust-derived melts (Fig. 4B), which is inconsistent with partial melting of the mafic lower crust. Furthermore, direct melting of the depleted mantle can also be excluded for the origin of the andesites studied here, since such andesites would have inherited the radiogenic isotopic signatures of the mantle peridotite instead of the enriched isotopic compositions observed in the Zenong andesites. In addition, the low MgO, Mg#, and compatible element (e.g., Cr and Ni) values of the Zenong andesites indicate that the depleted mantle is not an appropriate source for these volcanic rocks. In general, the mixing of crust-derived and mantle-derived melts could produce andesitic magmas; however, we suggest that magma-mixing is incompatible with the origin of the Zenong andesites, for the following reasons: (1) the lack of mafic enclaves and complex mineral zoning in the andesite samples (Figs. 2D and S4), (2) the presence of subparallel REE patterns in the basalt and andesite samples (Fig. 4D), and (3) relatively uniform Lu-Hf isotopic compositions (Fig. 6B).

The andesites are temporally and spatially associated with mantle-derived basalts and have a more evolved composition than primitive magmas. Thus, the andesites could have been derived from basaltic magmas, which had undergone various degrees of intra-crustal differentiation. A magmatic suite formed by fractional crystallization of a primitive magma commonly shows kink-shaped patterns in Zr versus SiO_2 and P_2O_5 versus SiO_2 diagrams (Figs. 7C and 7D; Lee and Bachmann, 2014). The Zr and P_2O_5 of studied andesites display an early decrease with increasing SiO_2, implying that the magma evolu-

tion was dominated by the wet cogenetic fractionation of plagioclase accompanied by hornblende and accessory minerals (Figs. 7C and 7D). Clinopyroxene in both andesite and basalt exhibit subparallel REE patterns. However, the clinopyroxene in the andesite displays three times the total REE contents and Eu depletion than the clinopyroxene in the basalt (Fig. 5B). The observed compositional change in the clinopyroxene is consistent with the incompatible elements enrichment and the Eu depletion during the compositional evolution of mantle-derived magma. Therefore, we suggest that the Zenong andesites were generated by crystallization differentiation of temporally and spatially coexisting basaltic magmas.

Origin of the Zenong Dacite and Rhyolite

Most felsic volcanic rocks from the Zenong Group have high SiO_2 (66.6–75.6 wt%) and low Mg# (14.4–36.9), suggesting that they were not directly formed by fractional crystallization of basaltic magma. In addition, the felsic volcanic rocks have relatively low Nb/U (3.0–5.5) and Ce/Pb (2.7–9.0) ratios, which are comparable to those of the average continental crust (Nb/U = 6.2, Ce/Pb = 3.9; Rudnick and Fountain, 1995), but significantly lower than those of mantle-derived oceanic island and mid-ocean ridge basalts (Nb/U = 47 ± 10 and Ce/Pb = 25 ± 5; Hofmann et al., 1986), supporting their crustal origin. Zircon Hf isotopic composition can provide robust constraints both on the source composition and the related magmatic processes of their host rocks (Belousova et al., 2006; Zhu et al., 2022). Significant zircon Hf isotopic variations within a sample could be a consequence of the decoupled release of zircon Hf and non-zircon Hf during crustal anatexis or magma mixing involving diverse sources (Tang et al., 2014; Griffin et al., 2002; Kemp et al., 2007). The Zenong felsic volcanic rocks show a limited range of negative $\varepsilon_{Hf}(t)$ values and normal mineral zoning (Fig. 6B), indicating that their parental magma was produced by partial melting of ancient continental crust. This is further supported by the enriched Sr−Nd isotopic compositions (Fig. 6A). Given that the central Lhasa subterrane is a microcontinent with an ancient crustal basement, the Zenong felsic volcanic rocks and the coeval plutonic rocks have similar enriched isotopic compositions and are most likely produced by partial melting of the lower continental crust (Chen et al., 2014, 2021).

A Transcrustal Magma Plumbing System

Mantle-derived mafic magma that underplates the lower continental crust at the mantle–crust interface can drive partial melting and assimilation while the magma undergoes fractional crystallization during subsequent magma storage and emplacement (Annen et al., 2006). The Zenong basalts have MgO contents of 6.1–3.1 wt%, and Cr and Ni contents of 96–0.8 ppm and 40–0.9 ppm, respectively (Table S3), all of which are lower than those of mantle-derived primary melts (MgO > 8 wt%, Cr > 750 ppm, and Ni > 300 ppm; Herzberg and O'Hara, 2002). This suggests that the parental magmas of the Zenong basalts have undergone crystal fractionation, most likely of mafic minerals (e.g., olivine and clinopyroxene), either in the magma chamber or en route to the surface (Pfänder et al., 2002). The substantial fractionation of clinopyroxene during the magmatic evolution is supported by the observation that a basalt sample (21-ZN-99) from the bottom of the Cishixiang section mainly consists of clinopyroxene and plagioclase and has a Cr content of 55 ppm, whereas a basalt sample (21-ZN-110) from the top of this section is mainly composed of plagioclase with subordinate clinopyroxene and has a much lower Cr content of 2.7 ppm (Table S3; Fig. 3). However, magma differentiation is thought to be dominated by clinopyroxene and chromite crystallization as reflected by Cr contents <250 ppm (Song et al., 2009). Overall, the Cr contents of the Zenong Group basalts are lower than 250 ppm (average 20 ppm; Table S3), suggesting olivine and clinopyroxene fractionation, as well as chromite crystallization. The plagioclase fractionation during magma differentiation is negligible because both the whole-rock and the clinopyroxene show insignificant Eu anomalies in the chondrite-normalized REE patterns (δEu = 0.90–1.05 for basalts, δEu = 0.90–1.05 for clinopyroxenes; Figs. 4D and 5B; Table S6).

As mentioned as mentioned in spatiotemporal distribution of the Zenong Group volcanic rocks, the andesites are temporally coeval and spatially coexisting with mantle-derived basalts and are thought to have been generated by fractional crystallization of basaltic parental magmas. The andesites have lower MgO (3.94–2.08 wt%) and Sr (395–188 ppm) contents (Table S3), and δEu (0.69−0.89) values (Fig. 4), implying that clinopyroxene and plagioclase were the major fractionating phases during magma differentiation in the deep crust. The REE pattern of the clinopyroxene in the andesites shows significant Eu negative anomalies when compared to clinopyroxene from the coexisting basalt (Fig. 4B), which is consistent with the separation of plagioclase in more evolved magmas.

Although temporally and spatially associated with intermediate to mafic volcanic rocks, the volumetrically dominant dacite and rhyolite are not generated by magma differentiation but are thought to be derived from partial melting of the lower continental crust. Mantle-derived basaltic magmas underplated the middle-lower crust and are thought to have provided enough heat and volatiles to trigger partial melting of the ancient continental basement. In this context, depleted mantle–derived materials are believed to have contaminated the Early Cretaceous (130–110 Ma) crust-derived magma, which is in accordance with the progressively depleted zircon Hf isotopic compositions during this period (Fig. 5).

Geodynamic Implications

The voluminous (>7000 km^2) Early Cretaceous volcanic−sedimentary Zenong Group is one of the most important constituents of the central Lhasa subterrane and, thus, provides crucial insight into the reconstruction of the Late Mesozoic orogenic evolution of central Tibet (Fig. 1). Previous studies revealed the presence of extensive Early Cretaceous (ca. 130−110 Ma) magmatic rocks in the central Lhasa subterrane (Fig. 1; Zhu et al., 2011; Li et al., 2018). However, the dynamic mechanism responsible for this magmatic event is disputed. It is generally accepted that the Early Cretaceous magmatic rocks in the central Lhasa terrane resulted from the northward low-angle or flat-slab subduction of the Neo-Tethys (Kapp and DeCelles, 2019). However, this model fails to account for the magmatic flare-up and the role of mantle melts in this extensive magmatic event. For instance, in Mexico, Peru, and Chile in South America, where flat-slab subduction is active, volcanism is insignificant or absent, and the overriding plates are characterized by low heat flow (Henry and Pollack, 1988; Manea et al., 2017). These features appear to argue against northward flat-slab subduction of the Neo-Tethys with respect to the intense magmatism in the central Lhasa subterranes. Some researchers proposed that the southward subduction and subsequent slab break-off of the Bangong-Nujiang ocean is responsible for the generation of the Early Cretaceous volcanic rocks in the central Lhasa subterrane (Zhu et al., 2009; Li et al., 2018; Chen et al., 2014). Although the timing of the closure of the Bangong-Nujiang ocean remains in dispute, it is generally believed that the Lhasa-Qiangtang collision occurred during the latest Jurassic–earliest Early Cretaceous (before ca. 132 Ma; Kapp et al., 2005; Murphy et al., 1997; Leier et al., 2007; Zhu et al., 2013; Ma et al., 2017; Hu et al., 2022; Song et al., 2024). Furthermore, slab break-off describes the detachment of a portion of the subducting slab, which can lead to localized magmatism but fails to account for

the widespread volcanism observed in the central Lhasa subterrane.

Bimodal volcanic suites generally occur in extensional settings related to intraplate, post-collisional, or backarc rifting tectonic regimes (Pin and Paquette, 1997; Shinjo and Kato, 2000; Chen et al., 2021). The Zenong basalts are characterized by minor LREE/HREE fractionation and low LREE contents, which is in contrast to the high LREE contents and strongly fractionated REE patterns of continental arc basalts (Xu et al., 2020). The Ti/V ratios of the mafic rocks studied here are between 20 and 50 and fall in an overlapping field of backarc basin basalt and MORB in the Ti versus V diagram (Fig. S5A; Shervais, 1982). The clinopyroxene composition in the mafic rocks provides a further constraint of the tectonic-magmatic affiliation of the Zenong basalts. Basaltic magmas in extensional settings (hotspot and rift) typically have low H_2O and O_2 fugacities relative to arc-axis magmas and are characterized by clinopyroxenes with relatively low Al_Z/TiO_2 (Al_Z = percentage of tetrahedral sites occupied by Al) ratios (Loucks, 1990). Therefore, subduction-related clinopyroxenes yield an Al_Z/TiO_2 trend that is roughly twice as steep as that defined by clinopyroxenes from rift settings in an Al_Z versus TiO_2 diagram (Fig. S5B). Most clinopyroxenes from the Zenong Group basalts and andesites plot in the rift-related compositional field due to their low Al_Z/TiO_2. The variable TiO_2 and Cr_2O_3, and Al_2O_3 contents of the clinopyroxenes provide further evidence that the Zenong Group basalts share similar geochemical affinities with island arc tholeiitic lavas and backarc basin basalts (Fig. S5C). Therefore, we suggest a backarc rift model to account for the petrogenesis of the Early Cretaceous magmatic rocks in central Lhasa. This model can readily explain several geological facts:

(1) Sedimentary environment: In the Xigaze forearc basin, the Early Cretaceous (113–110 Ma) Chongdui Formation turbidites unconformably overlay the ophiolitic basement (ca. 131–124 Ma; Wang et al., 2017), indicating an extension-related basin filled with marine clastic sediments (Fig. 8). In the Linzhou basin of southern Lhasa, the Early Cretaceous Takena and Shexing Formations document an upward transition from shallow-marine carbonates to fluvial sediments (lower part of the Shexing Formation), implying marine regression and initial topographic growth of the Gangdese arc (Leier et al., 2007). In comparison, the Early Cretaceous Zenong Group in central Lhasa is mainly composed of volcanic−sedimentary rocks that unconformably overly the continental basement of the Permian Laga Formation (Fig. 3B). The association of volcanic assemblages with limestone is indicative of a gradually shallowing marine environment. Conversely, the Early Cretaceous (116−99 Ma) shallow-sea Langshan Formation in northern Lhasa overlies the Early Cretaceous (125−116 Ma) Duoni Formation (shelf-fan delta) and is in turn unconformably overlain by thick conglomerate-bearing deposits (Jinzhushan and Daxiong Formation in the Baingoin and Coqen area, respectively; Fig. 8; Xu et al., 2022). The variation and difference in the sedimentary environment from south to north suggest that the Lhasa terrane underwent contemporaneous uplift and subsidence.

(2) Magma composition: The Yanhu volcanic rocks (131–116 Ma) in northern Lhasa are potassium-rich, which is indicative of a collision-related or post-collisional setting rather than a subduction environment (Table S7; Li et al., 2018). Furthermore, the late Early Cretaceous (114–109 Ma) volcanic rocks in the Yanhu and Nagqu areas are characterized by bimodal and high-K calc-alkaline to shoshonitic volcanic rocks (Table S7; Sui et al., 2013). Coeval (134–109 Ma) plutonic rocks in northern Lhasa mainly have weak peraluminous to peraluminous compositions (Table S7; Zhu et al., 2016; Sun et al., 2015b). The magmatic rock assemblages in northern Lhasa are similar to those in

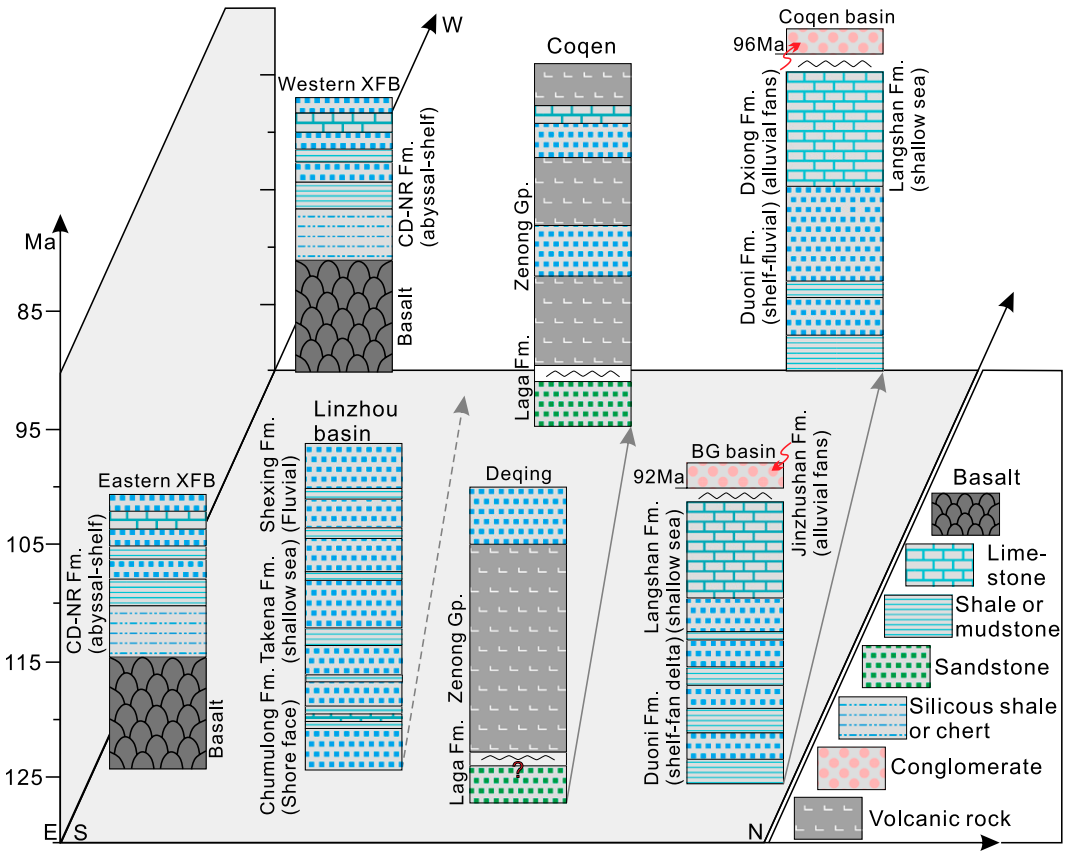

Figure 8. Stratigraphy and facies comparison among principal Cretaceous basins on the Lhasa block. Sources of stratigraphic data: Xigaze Forearc Basin (XFB) by An et al. (2014) and Wang et al. (2017); Linzhou Basin by Wang et al. (2020); Coqen Basin by Sun et al. (2015a); Baingoin Basin (BG) from Lai et al. (2019a). CD-NR Fm.—Chongdui-Ngamring Formation.

some extensional basins, which display unique combinations of calc-alkaline or tholeiitic to calc-alkaline and peraluminous magmatism, especially felsic components (Rahimzadeh et al., 2021). The systematic study of the potassium-rich Early Cretaceous (126–110 Ma) lavas in central Lhasa reveals their compositional bimodality, indicative of within-plate geochemical signatures. Contemporary plutonic rocks (122–113 Ma) in central Lhasa are characterized by arc-like high-K calc-alkaline granites and tholeiitic gabbro with oceanic-island basalt–like REE patterns. Conversely, sporadic Early Cretaceous (122–114 Ma) intrusive rocks in southern Lhasa have arc-like magma compositions, including positive zircon $\varepsilon_{Hf}(t)$ values, and calc-alkaline and adakitic affinities (Table S7; Wang et al., 2013, 2022). Consequently, the compositional variation of magmatism from the south to the north of the Lhasa terrane can be explained by arc and backarc rift assemblage.

(3) Crustal thinning: The central Lhasa Late Jurassic to Early Cretaceous (165–135 Ma) magmatic rocks (including volcanic rocks and intrusive rocks) have high $(La/Yb)_N$ values (25–4.5) with an average value of 10 (Fig. S6), thereby suggesting that they formed in the thickened crust (ca. 50 km). The negative zircon $\varepsilon_{Hf}(t)$ values and high SiO_2 contents of these magmatic rocks indicate an origin involving the anatexis of ancient thickened crust. In contrast, the Early Cretaceous (130–110 Ma) magmatic rocks (including mafic to acidic intrusive rocks and the volcanic counterparts) in central Lhasa have low $(La/Yb)_N$ values (15–2) with an average value of 6.5 (Fig. S6), indicating that their origin was related to crustal thinning (~40 km). The direct source of mantle materials, coupled with gradually positive zircon $\varepsilon_{Hf}(t)$ values would require a decompressive environment and increased mantle contribution to the Early Cretaceous magmatic rocks. Therefore, the findings of this study provide robust evidence for a backarc rift setting of the Early Cretaceous magmatism in central Lhasa.

Generation and Evolution of Backarc Rift

The origin of the central Lhasa subterrane is still widely debated. Some researchers argue for a continental arc origin related to the southward subduction of the Bangong-Nujiang ocean (Li et al., 2018), while others favor a foreland basin origin after the collision of the Lhasa and Qiangtang terranes (Leeder et al., 1988; Kapp et al., 2007). A synthesized analysis of the sedimentary rocks and sequences, the nature of the basement underlying the central Lhasa subterrane, and new geochemical data for the spatial and temporal variations of magmatic rocks are needed to provide sufficient new information to elaborate the origin of the central Lhasa terrane.

Geochemical data reveal that the calc-alkaline volcanic rocks (137–130 Ma) in the southern Lhasa subterrane (also called Gangdese arc) provide a magmatic record corresponding to the northward, high-angle subduction of the Neo-Tethyan oceanic lithosphere beneath the Gangdese arc during the Early Cretaceous (Zhu et al., 2009). Subsequently, the reduction of the convergence rate of the Indo-Asian plates (Cande and Stegman, 2011) lead to a magmatic lull (130–110 Ma) in the Gangdese arc (Fig. 9), probably due to subduction rollback of the Neo-Tethyan oceanic plate, corresponding to the period of the forearc extension and the birth of the Xigaze forearc basin (Fig. 10A; Wang et al., 2017). In contrast, contemporaneous (130–110 Ma) magmatic rocks occur widely in central and northern Lhasa subterranes (Figs. 1, 9, and 10A), suggesting that the magmatic front moved farther north due to slab rollback. Asthenospheric mantle upwelling triggers lithospheric thinning and backarc basin opening during the Early Cretaceous (Figs. 9 and 10A). The Early Cretaceous volcano-sedimentary features in central and northern Lhasa are similar to those in the rift systems of the Songpan-Garze Terrane and the western Yangtze Block where volcanic rocks unconformably overlie the continental basement, while pelagic deposits and deep-water turbidites are absent (Wang et al., 2019; Liu and Wang, 2023). However, this extensional setting did not extend into the late Early Cretaceous. This is evidenced by the acceleration of the convergence rate of the Indo-Asian plates (Cande and Stegman, 2011), the migration of the magmatic front from central and northern Lhasa to southern Lhasa subterranes, and the massive exposure of granites in the Gangdese arc since ca. 110 Ma (Figs. 1 and 10B; Ji et al., 2009; Chapman and Kapp, 2017b; Zhu et al., 2022). A strong compression probably occurred after the end of the Early Cretaceous magmatic activities and is documented by widespread early Late Cretaceous conglomerate sedimentation in the Lhasa terrane.

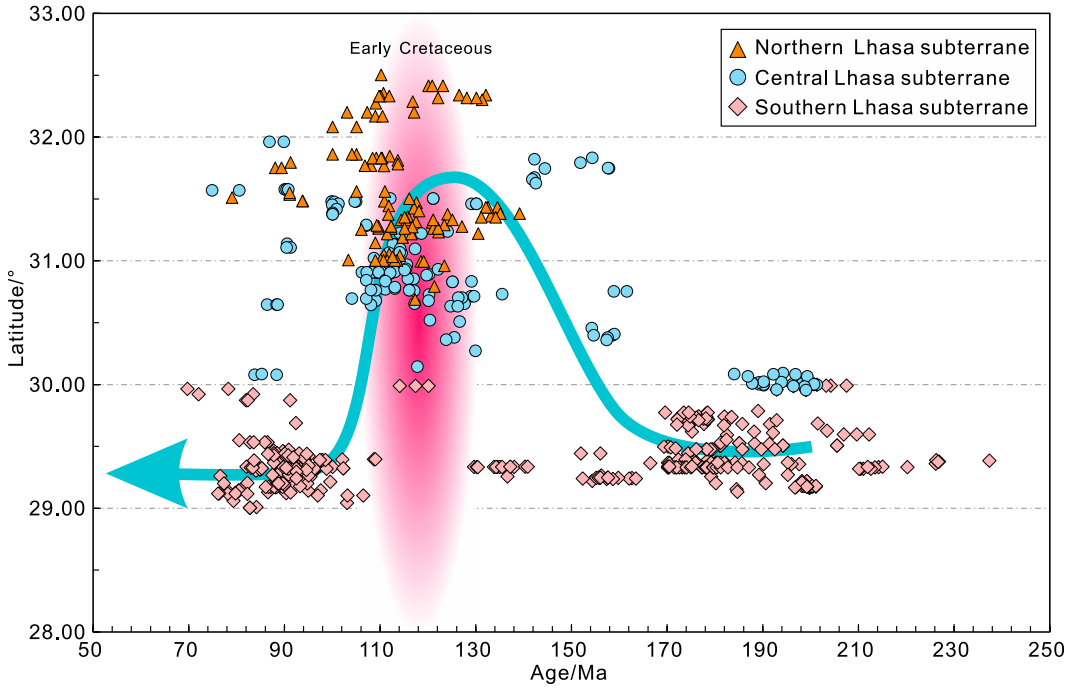

Figure 9. Temporal and spatial distribution of Mesozoic magmatic rocks in the Lhasa terrane (see Table S8 for data source; see text footnote 1). The magmatic rocks migrate northward at ca. 130–110 Ma and southward at ca. 110 Ma.

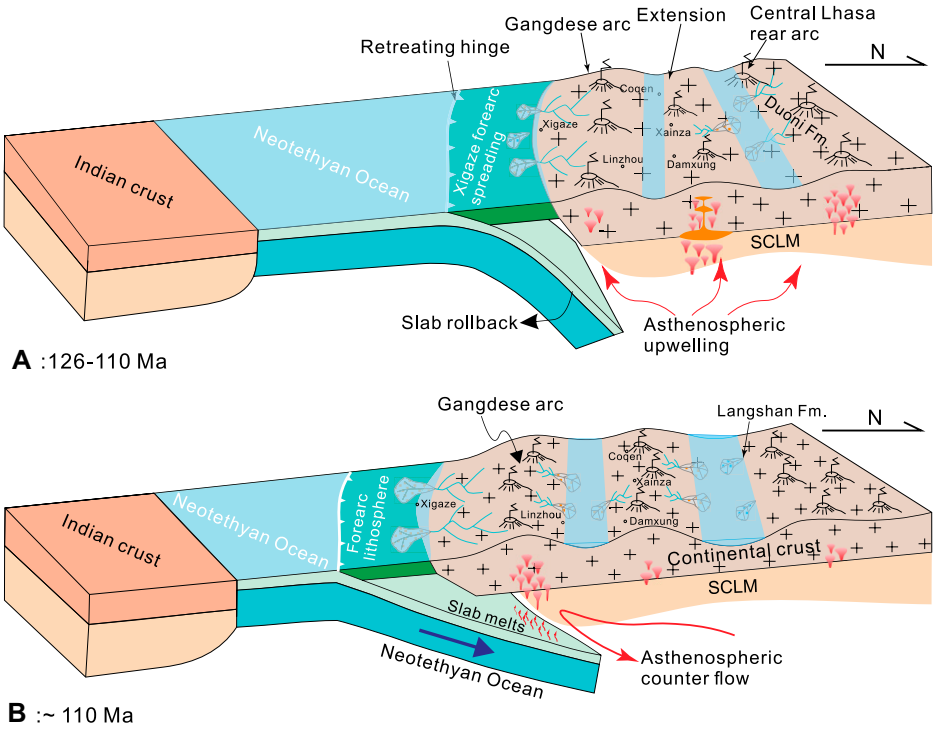

Figure 10. (A, B) Simplified cross section of the Early Cretaceous convergent margin of the Lhasa terrane, showing different magmatic pulses at >130 Ma, 130–110 Ma, and ca. 110 Ma in the Lhasa terrane. These panels emphasize the positions of the magmatic front (MF) and backarc (BA); slab fluids triggering MF magmatism vs. decompression melting triggering BA magmatism; and subcontinental lithospheric mantle (SCLM) and melting-differentiation-mixing processes beneath both MF and BA. Small wavy red lines in B show the trajectory of slab fluids whereas continuous red lines in A and B show asthenospheric mantle flow.

CONCLUSIONS

The volcanic rocks of the Zenong Group in central Lhasa are characterized by compositional bimodality in volcanic rock sections and erupted from 126 Ma to 105 Ma. The basalts were mostly derived from low-degree partial melting of a lithospheric mantle in the spinel stability field, with minor input of melt from an asthenospheric mantle. The andesites were generated by crystallization differentiation of temporally and spatially coexisting basaltic magmas, while the dacites and rhyolites are interpreted to have originated from the partial melting of ancient lower crust. The compositional bimodality of volcanic rocks coupled with their arc-like and within-plate-like geochemical features indicate that the Zenong Group volcanic rocks were derived from the melting of multiple sources during the Early Cretaceous backarc extension triggered by subduction rollback of the Neo-Tethyan oceanic plate.

ACKNOWLEDGMENTS

This work was supported by the National Natural Science Foundation of China (grants 42488201, 42402066) and Jiangxi Provincial Natural Science Foundation (grant 20242BAB21019). This paper benefited from the inspiring discussion with De-hong Du, Wen Lai, Shi-lei Qiao, and Wei Jiang. We are much indebted to Science Editor Mihai Ducea for his efficient handling and to Xuxuan Ma and Camilo Bustamante for their critical and constructive comments, which strengthened this manuscript greatly.

REFERENCES CITED

An, W., Hu, X., Garzanti, E., BouDagher-Fadel, M.K., Wang, J., and Sun, G., 2014, Xigaze forearc basin revisited (South Tibet): Provenance changes and origin of the Xigaze Ophiolite: Geological Society of America Bulletin, v. 126, p. 1595–1613, https://doi.org/10.1130/B31020.1.

Annen, C., Blundy, J., and Sparks, R., 2006, The genesis of intermediate and silicic magmas in deep crustal hot zones: Journal of Petrology, v. 47, p. 505–539, https://doi.org/10.1093/petrology/egi084.

Belousova, E.A., Griffin, W.L., O'Reilly, S.Y., and Fisher, N.L., 2002, Igneous zircon: Trace element composition as an indicator of source rock type: Contributions to Mineralogy and Petrology, v. 143, p. 602–622, https://doi.org/10.1007/s00410-002-0364-7.

Belousova, E.A., Griffin, W.L., and O'Reilly, S.Y., 2006, Zircon crystal morphology, trace element signatures and Hf isotope composition as a tool for petrogenetic modelling: Examples from Eastern Australian granitoids: Journal of Petrology, v. 47, p. 329–353, https://doi.org/10.1093/petrology/egi077.

Bienvenu, P., Bougault, H., Joron, M., and Dmitriev, L., 1990, MORB alteration: Rare-earth element/non-rare earth hygromagmaphile element fractionation: Chemical Geology, v. 82, p. 1–14, https://doi.org/10.1016/0009-2541(90)90070-N.

Bustamante, C., Archanjo, C.J., Cardona, A., and Vervoort, J.D., 2016, Late Jurassic to Early Cretaceous plutonism in the Colombian Andes: A record of long-term arc maturity: Geological Society of America Bulletin, v. 128, p. 1762–1779, https://doi.org/10.1130/B31307.1.

Cande, S.C., and Stegman, D.R., 2011, Indian and African plate motions driven by the push force of the Reunion plume head: Nature, v. 475, p. 47–52, https://doi.org/10.1038/nature10174.

Castro, A., 2013, Tonalite–granodiorite suites as cotectic systems: A review of experimental studies with applications to granitoid petrogenesis: Earth-Science Reviews, v. 124, p. 68–95, https://doi.org/10.1016/j.earscirev.2013.05.006.

Castro, A., Rodriguez, C., Fernández, C., Aragón, E., Pereira, M.F., and Molina, J.F., 2021, Secular variations of magma source compositions in the North Patagonian batholith from the Jurassic to Tertiary: Was mélange melting involved?: Geosphere, v. 17, p. 766–785, https://doi.org/10.1130/GES02338.1.

Chapman, J.B., and Kapp, P., 2017, Tibetan magmatism database: Geochemistry, Geophysics, Geosystems, v. 18, p. 4229–4234, https://doi.org/10.1002/2017GC007217.

Chapman, J.B., Ducea, M.N., Kapp, P., Gehrels, G.E., and DeCelles, P.G., 2017, Spatial and temporal radiogenic isotopic trends of magmatism in Cordilleran orogens: Gondwana Research, v. 48, p. 189–204, https://doi.org/10.1016/j.gr.2017.04.019.

Chapman, J.B., Scoggin, S.H., Kapp, P., Carrapa, B., Ducea, M.N., Worthington, J., Oimahmadov, I., and Gadoev, M., 2018, Mesozoic to Cenozoic magmatic history of the Pamir: Earth and Planetary Science Letters, v. 482, p. 181–192, https://doi.org/10.1016/j.epsl.2017.10.041.

Chen, S.S., Fan, W.M., Shi, R.D., Xu, J.F., Yang, K., and Pan, Z., 2021, Early Cretaceous volcanic rocks in Yunzhug area, central Tibet, China, associated with arc–continent collision in the Tibetan Plateau?: Lithos, v. 380, https://doi.org/10.1016/j.lithos.2020.105827.

Chen, Y., Zhu, D.C., Zhao, Z., Meng, F.Y., Wang, Q., Santosh, M., Wang, L.Q., Dong, G.C., and Mo, X.X., 2014, Slab breakoff triggered ca. 113 Ma magmatism around Xainza area of the Lhasa Terrane, Tibet: Gondwana Research, v. 26, p. 449–463, https://doi.org/10.1016/j.gr.2013.06.005.

Clemens, J.D., Stevens, G., and Farina, F., 2011, The enigmatic sources of I-type granites: The peritectic connexion: Lithos, v. 126, p. 174–181, https://doi.org/10.1016/j.lithos.2011.07.004.

Collins, W.J., Belousova, E.A., Kemp, A.I., and Murphy, J.B., 2011, Two contrasting Phanerozoic orogenic systems revealed by hafnium isotope data: Nature Geoscience, v. 4, p. 333–337, https://doi.org/10.1038/ngeo1127.

Coulon, C., Maluski, H., Bollinger, C., and Wang, S., 1986, Mesozoic and Cenozoic volcanic rocks from central and southern Tibet: ^{39}Ar-^{40}Ar dating, petrological characteristics and geodynamical significance: Earth and Planetary Science Letters, v. 79, p. 281–302, https://doi.org/10.1016/0012-821X(86)90186-X.

DeCelles, P.G., Ducea, M.N., Kapp, P., and Zandt, G., 2009, Cyclicity in Cordilleran orogenic systems: Nature Geoscience, v. 2, p. 251–257, https://doi.org/10.1038/ngeo469.

Deng, J., Liu, X., Wang, Q., Dilek, Y., and Liang, Y., 2017, Isotopic characterization and petrogenetic modeling of Early Cretaceous mafic diking—Lithospheric extension in the North China craton, eastern Asia: Geological Society of America Bulletin, v. 129, p. 1379–1407, https://doi.org/10.1130/B31609.1.

Duggen, S., Hoernle, K., Bogaard, P., and Garbe-Schonberg, D., 2005, Post-collisional transition from subduction to intra-plate type magmatism in the westernmost Mediterranean: Evidence for continental edge delamination of subcontinental lithosphere: Journal of Petrology, v. 46, p. 1155–1201, https://doi.org/10.1093/petrology/egi013.

Foley, S.F., Jackson, S.E., Fryer, B.J., Greenouch, J.D., and Jenner, G.A., 1996, Trace element partition coefficients for clinopyroxene and phlogopite in an alkaline lamprophyre from Newfoundland by LAM-ICP-MS: Geochimica et Cosmochimica Acta, v. 60, p. 629–638, https://doi.org/10.1016/0016-7037(95)00422-X.

Forni, F., Degruyter, W., Bachmann, O., De Astis, G., and Mollo, S., 2018, Long-term magmatic evolution reveals the beginning of a new caldera cycle at Campi Flegrei: Science Advances, v. 4, https://doi.org/10.1126/sciadv.aat9401.

Furman, T., and Graham, D., 1999, Erosion of lithospheric mantle beneath the East African Rift system: Geochemical evidence from the Kivu volcanic province: Lithos, v. 48, p. 237–262, https://doi.org/10.1016/S0024-4937(99)00031-6.

Gibson, I.L., Kirkpatrick, R.J., Emmerman, R., Schmincke, H.U., Pritchard, G., Oakley, P.J., Thorpe, R.S., and Marriner, G.F., 1982, The trace element composition of the lavas and dikes from a 3-km vertical section through the lava pile of eastern Iceland: Journal of Geophysical Research: Solid Earth, v. 87, p. 6532–6546, https://doi.org/10.1029/JB087iB08p06532.

Griffin, W.L., Wang, X., Jackson, S.E., Pearson, N.J., O'Reilly, S.Y., Xu, X., and Zhou, X., 2002, Zircon chemistry and magma mixing, SE China: in-situ analysis of Hf isotopes, Tonglu and Pingtan igneous complexes: Lithos, v. 61, p. 237–269, https://doi.org/10.1016/S0024-4937(02)00082-8.

Grove, T.L., Elkins-Tanton, L.T., Parman, S.W., Chatterjee, N., Müntener, O., and Gaetani, G.A., 2003, Fractional crystallization and mantle-melting controls on calc-alkaline differentiation trends: Contributions to Mineralogy and Petrology, v. 145, p. 515–533, https://doi.org/10.1007/s00410-003-0448-z.

Guo, F., Wu, Y., Zhang, B., Zhang, X., Zhao, L., and Liao, J., 2021, Magmatic responses to Cretaceous subduction and tearing of the paleo-Pacific plate in SE China: An overview: Earth-Science Reviews, v. 212, https://doi.org/10.1016/j.earscirev.2020.103448.

Henry, S.G., and Pollack, H.N., 1988, Terrestrial heat flow above the Andean subduction zone in Bolivia and Peru: Journal of Geophysical Research: Solid Earth, v. 93, p. 15,153–15,162, https://doi.org/10.1029/JB093iB12p15153.

Herzberg, C., and O'Hara, M.J., 2002, Plume-associated ultramafic magmas of Phanerozoic age: Journal of Petrology, v. 43, p. 1857–1883, https://doi.org/10.1093/petrology/43.10.1857.

Hildreth, W., and Moorbath, S., 1988, Crustal contributions to arc magmatism in the Andes of Central Chile: Contributions to Mineralogy and Petrology, v. 98, p. 455–489, https://doi.org/10.1007/BF00372365.

Hofmann, A.W., Jochum, K.P., Seufert, M., and White, W.M., 1986, Nb and Pb in oceanic basalts: new constraints on mantle evolution: Earth and Planetary Science Letters, v. 79, p. 33–45, https://doi.org/10.1016/0012-821X(86)90038-5.

Hu, X., Ma, A., Xue, W., Garzanti, E., Cao, Y., Li, S.M., Sun, G.Y., and Lai, W., 2022, Exploring a lost ocean in the Tibetan Plateau: Birth, growth, and demise of the Bangong-Nujiang Ocean: Earth-Science Reviews, v. 229, https://doi.org/10.1016/j.earscirev.2022.104031.

Ji, W.Q., Wu, F.Y., Chung, S.L., Li, J.X., and Liu, C.Z., 2009, Zircon U–Pb geochronology and Hf isotopic constraints on petrogenesis of the Gangdese batholith, southern Tibet: Chemical Geology, v. 262, p. 229–245, https://doi.org/10.1016/j.chemgeo.2009.01.020.

Kapp, P., and DeCelles, P.G., 2019, Mesozoic–Cenozoic geological evolution of the Himalayan-Tibetan orogen and working tectonic hypotheses: American Journal of Science, v. 319, p. 159–254, https://doi.org/10.2475/03.2019.01.

Kapp, P., Murphy, M.A., Yin, A., Harrison, T.M., Ding, L., and Guo, J., 2003, Mesozoic and Cenozoic tectonic evolution of the Shiquanhe area of western Tibet: Tectonics, v. 22, https://doi.org/10.1029/2001TC001332.

Kapp, P., Yin, A., Harrison, T.M., and Ding, L., 2005, Cretaceous-Tertiary shortening, basin development, and volcanism in central Tibet: Geological Society of America Bulletin, v. 117, p. 865–878, https://doi.org/10.1130/B25595.1.

Kapp, P., DeCelles, P.G., Gehrels, G.E., Heizler, M., and Ding, L., 2007, Geological records of the Lhasa-Qiangtang and Indo-Asian collisions in the Nima area of central Tibet: Geological Society of America Bulletin, v. 119, p. 917–933, https://doi.org/10.1130/B26033.1.

Kay, R.W., 1978, Aleutian magnesian andesites: Melts from subducted Pacific Ocean crust: Journal of Volcanology and Geothermal Research, v. 4, p. 117–132, https://doi.org/10.1016/0377-0273(78)90032-X.

Kelemen, P.B., 1986, Assimilation of ultramafic rock in subduction-related magmatic arcs: The Journal of Geology, v. 94, p. 829–843, https://doi.org/10.1086/629090.

Kemp, A.I.S., Hawkesworth, C.J., Foster, G.L., Paterson, B.A., Woodhead, J.D., Hergt, J.M., Gray, C.M., and Whitehouse, M.J., 2007, Magmatic and crustal differentiation history of granitic rocks from Hf-O isotopes in zircon: Science, v. 315, p. 980–983, https://doi.org/10.1126/science.1136154.

Kushiro, I., 1975, Carbonate-silicate reactions at high pressures and possible presence of dolomite and magnesite in the upper mantle: Earth and Planetary Science Letters, v. 28, p. 116–120, https://doi.org/10.1016/0012-821X(75)90218-6.

Lai, W., Hu, X., Garzanti, E., Sun, G., Garzione, C.N., Fadel, M.B., and Ma, A., 2019a, Initial growth of the northern Lhasaplano, Tibetan Plateau in the early Late Cretaceous (ca. 92 Ma): Geological Society of America Bulletin, v. 131, p. 1823–1836, https://doi.org/10.1130/B35124.1.

Lai, W., Hu, X., Garzanti, E., Xu, Y., Ma, A., and Li, W., 2019b, Early Cretaceous sedimentary evolution of the northern Lhasa terrane and the timing of initial Lhasa-Qiangtang collision: Gondwana Research, v. 73, p. 136–152, https://doi.org/10.1016/j.gr.2019.03.016.

Lee, C.T.A., and Bachmann, O., 2014, How important is the role of crystal fractionation in making intermediate magmas? Insights from Zr and P systematics: Earth and Planetary Science Letters, v. 393, p. 266–274, https://doi.org/10.1016/j.epsl.2014.02.044.

Leeder, M.R., Smith, A.B., and Yin, J.X., 1988, Sedimentology, palaeoecology and palaeoenvironmental evolution of the 1985 Lhasa to Golmud Geotraverse: Philosophical Transactions of the Royal Society of London A: Mathematical, Physical and Engineering Sciences, v. 327, p. 107–143, https://doi.org/10.1098/rsta.1988.0123.

Leier, A.L., DeCelles, P.G., Kapp, P., and Ding, L., 2007, The Takena Formation of the Lhasa terrane, southern Tibet: The record of a Late Cretaceous retroarc foreland basin: Geological Society of America Bulletin, v. 119, p. 31–48, https://doi.org/10.1130/B25974.1.

Li, M.J., Zeng, Y.C., Tiepolo, M., Farina, F., Xu, J.F., Huang, F., Liu, X.-J., Chen, Q., and Ma, Y., 2023, Grain-scale zircon Hf isotope heterogeneity inherited from sediment-metasomatized mantle: Geochemical and Nd-Hf-Pb-O isotopic constraints on Early Cretaceous intrusions in central Lhasa Terrane, Tibetan Plateau: American Mineralogist, v. 108, p. 1692–1707, https://doi.org/10.2138/am-2022-8508.

Li, S.M., Wang, Q., Zhu, D.C., Stern, R.J., Cawood, P.A., Sui, Q.L., and Zhao, Z., 2018, One or two Early Cretaceous arc systems in the Lhasa Terrane, southern Tibet: Journal of Geophysical Research: Solid Earth, v. 123, p. 3391–3413, https://doi.org/10.1002/2018JB015582.

Liu, S., and Wang, Y., 2023, Origin of the Songpan-Garze Terrane on the northeastern Tibetan Plateau, eastern segment of the Tethyan tectonic domain: A Middle Permian–Early Triassic intracontinental rifting system: Geological Society of America Bulletin, v. 135, p. 1993–2014, https://doi.org/10.1130/B36468.1.

Liu, Y., Hu, Z., Gao, S., Günther, D., Xu, J., Gao, C., and Chen, H., 2008, In situ analysis of major and trace elements of anhydrous minerals by LA-ICP-MS without applying an internal standard: Chemical Geology, v. 257, p. 34–43, https://doi.org/10.1016/j.chemgeo.2008.08.004.

Loucks, R.R., 1990, Discrimination of ophiolitic from nonophiolitic ultramafic-mafic allochthons in orogenic belts by the Al/Ti ratio in clinopyroxene: Geology, v. 18, p. 346–349, https://doi.org/10.1130/0091-7613(1990)018<0346:DOOFNU>2.3.CO;2.

Ludwig, K.R., 2012, User's Manual for Isoplot Version 3.75–4.15: A Geochronological Toolkit for Microsoft Excel: Berkeley Geochronological Center Special Publication 5, 75 p.

Lustrino, M., 2005, How the delamination and detachment of lower crust can influence basaltic magmatism: Earth-Science Reviews, v. 72, p. 21–38, https://doi.org/10.1016/j.earscirev.2005.03.004.

Ma, A., Hu, X., Garzanti, E., Han, Z., and Lai, W., 2017, Sedimentary and tectonic evolution of the southern Qiangtang basin: Implications for the Lhasa-Qiangtang collision timing: Journal of Geophysical Research: Solid Earth, v. 122, p. 4790–4813, https://doi.org/10.1002/2017JB014211.

Ma, L., Jiang, S.Y., Hofman, A.W., Dai, B.Z., Hou, M.L., Zhao, K.D., Chen, L.H., Li, W.J., and Jiang, H.Y., 2014, Lithospheric and asthenospheric sources of lamprophyres in the Jiaodong Peninsula: A consequence of rapid lithospheric thinning beneath the North China Craton?: Geochimica et Cosmochimica Acta, v. 124, p. 250–271, https://doi.org/10.1016/j.gca.2013.09.035.

Ma, X., Xu, Z., Meert, J.G., Tian, Z., and Li, H., 2021, Early Eocene high-flux magmatism and concurrent high-temperature metamorphism in the Gangdese belt, southern Tibet: Geological Society of America Bulletin, v. 133, p. 1194–1216, https://doi.org/10.1130/B35770.1.

Manea, V.C., Manea, M., Ferrari, L., Orozco-Esquivel, T., Valenzuela, R.W., Husker, A., and Kostoglodov, V., 2017, A review of the geodynamic evolution of flat slab subduction in Mexico, Peru, and Chile: Tectonophysics, v. 695, p. 27–52, https://doi.org/10.1016/j.tecto.2016.11.037.

Middlemost, E.A., 1994, Naming materials in the magma/igneous rock system: Earth-Science Reviews, v. 37, p. 215–224, https://doi.org/10.1016/0012-8252(94)90029-9.

Mo, X., Niu, Y., Dong, G., Zhao, Z., Hou, Z., Zhou, S., and Ke, S., 2008, Contribution of syncollisional felsic magmatism to continental crust growth: A case study of the Paleogene Linzizong volcanic succession in southern Tibet: Chemical Geology, v. 250, p. 49–67, https://doi.org/10.1016/j.chemgeo.2008.02.003.

Murphy, M.A., Yin, A., Harrison, T.M., Durr, S.B., Ryerson, F.J., and Kidd, W.S.F., 1997, Did the Indo-Asian collision alone create the Tibetan Plateau?: Geology, v. 25, p. 719–722, https://doi.org/10.1130/0091-7613(1997)025<0719:DTIACA>2.3.CO;2.

Pan, G.T., 2006, Spatial temporal framework of the Gangdese Orogenic Belt and its evolution: Acta Petrologica Sinica (Yanshi Xuebao), v. 22, p. 521–533.

Pfänder, J.A., Jochum, K., Kozakov, I., Kröner, A., and Todt, W., 2002, Coupled evolution of back-arc and island arc-like mafic crust in the late-Neoproterozoic Agardagh Tes-Chem ophiolite, Central Asia: Evidence from trace element and Sr–Nd–Pb isotope data: Contributions to Mineralogy and Petrology, v. 143, p. 154–174, https://doi.org/10.1007/s00410-001-0340-7.

Pin, C., and Paquette, J.L., 1997, A mantle-derived bimodal suite in the Hercynian Belt: Nd isotope and trace element evidence for a subduction-related rift origin of the Late Devonian Brévenne metavolcanics, Massif Central (France): Contributions to Mineralogy and Petrology, v. 129, p. 222–238, https://doi.org/10.1007/s004100050334.

Plank, T., 2005, Constraints from thorium/lanthanum on sediment recycling at subduction zones and the evolution of the continents: Journal of Petrology, v. 46, p. 921–944, https://doi.org/10.1093/petrology/egi005.

Polat, A., and Hofmann, A., 2003, Alteration and geochemical patterns in the 3.7–3.8 Ga Isua greenstone belt, West Greenland: Precambrian Research, v. 126, p. 197–218, https://doi.org/10.1016/S0301-9268(03)00095-0.

Polat, A., Hofmann, A., and Rosing, M.T., 2002, Boninite-like volcanic rocks in the 3.7–3.8 Ga Isua greenstone belt, West Greenland: geochemical evidence for intra-oceanic subduction zone processes in the early Earth: Chemical Geology, v. 184, p. 231–254, https://doi.org/10.1016/S0009-2541(01)00363-1.

Putirka, K.D., 2008, Thermometers and barometers for volcanic systems: Reviews in Mineralogy and Geochemistry, v. 69, p. 61–120, https://doi.org/10.2138/rmg.2008.69.3.

Rahimzadeh, B., Mahmoudi, S., Corfu, F., Ahadnejad, V., and Von Quadt, A., 2021, A unique period of bimodal volcanism at 130–110 Ma in the northern Sanandaj-Sirjan Zone: Evidence for an extensional setting: Lithos, v. 392–393, https://doi.org/10.1016/j.lithos.2021.106155.

Rapp, R.P., and Watson, E.B., 1995, Dehydration melting of metabasalt at 8–32 kbar: implications for continental growth and crust-mantle recycling: Journal of

Petrology, v. 36, p. 891–931, https://doi.org/10.1093/petrology/36.4.891.

Rapp, R.P., Shimizu, N., Norman, M.D., and Applegate, G.S., 1999, Reaction between slab-derived melts and peridotite in the mantle wedge: Experimental constraints at 3.8 GPa: Chemical Geology, v. 160, p. 335–356, https://doi.org/10.1016/S0009-2541(99)00106-0.

Rudnick, R.L., and Fountain, D.M., 1995, Nature and composition of the continental crust: A lower crustal perspective: Reviews of Geophysics, v. 33, p. 267–309, https://doi.org/10.1029/95RG01302.

Sharples, W., Jadamec, M.A., Moresi, L.N., and Capitanio, F.A., 2014, Overriding plate controls on subduction evolution: Journal of Geophysical Research: Solid Earth, v. 119, p. 6684–6704, https://doi.org/10.1002/2014JB011163.

Shervais, J.W., 1982, Ti-V plots and the petrogenesis of modern and ophiolitic lavas: Earth and Planetary Science Letters, v. 59, p. 101–118, https://doi.org/10.1016/0012-821X(82)90120-0.

Shinjo, R., and Kato, Y., 2000, Geochemical constraints on the origin of bimodal magmatism at the Okinawa Trough, an incipient back-arc basin: Lithos, v. 54, p. 117–137, https://doi.org/10.1016/S0024-4937(00)00034-7.

Sisson, T.W., and Grove, T.L., 1993, Experimental investigations of the role of H_2O in calc-alkaline differentiation and subduction zone magmatism: Contributions to Mineralogy and Petrology, v. 113, p. 143–166, https://doi.org/10.1007/BF00283225.

Song, P., Ding, L., Li, J., Yue, Y., and Xie, J., 2024, Unraveling the Lhasa-Qiangtang collision in western Tibet: Insights from geochronological and paleomagnetic analyses: Geophysical Research Letters, v. 51, https://doi.org/10.1029/2024GL110264.

Song, X.Y., Keays, R.R., Xiao, L., Qi, H.W., and Ihlenfeld, C., 2009, Platinum-group element geochemistry of the continental flood basalts in the central Emeishan Large Igneous Province, SW China: Chemical Geology, v. 262, p. 246–261, https://doi.org/10.1016/j.chemgeo.2009.01.021.

Staudigel, H., Plank, T., White, B., and Schmincke, H.U., 1996, Geochemical fluxes during seafloor alteration of the basaltic upper oceanic crust: DSDP Sites 417 and 418, *in* Bebout, G.E., et al., eds., Subduction: Top to Bottom: American Geophysical Union, Geophysical Monograph Series, v. 96, p. 19–38, https://doi.org/10.1029/GM096p0019.

Sui, Q.L., Wang, Q., Zhu, D.C., Zhao, Z.D., Chen, Y., Santosh, M., Hu, Z.C., Yuan, H.L., and Mo, X.X., 2013, Compositional diversity of ca. 110 Ma magmatism in the northern Lhasa Terrane, Tibet: Implications for the magmatic origin and crustal growth in a continent–continent collision zone: Lithos, v. 168, p. 144–159, https://doi.org/10.1016/j.lithos.2013.01.012.

Sun, G., Hu, X., Sinclair, H.D., BouDagher-Fadel, M.K., and Wang, J., 2015a, Late Cretaceous evolution of the Coqen Basin (Lhasa terrane) and implications for early topographic growth on the Tibetan Plateau: Geological Society of America Bulletin, v. 127, p. 1001–1020, https://doi.org/10.1130/B31137.1.

Sun, G., Hu, X., and Sinclair, H.D., 2017, Early cretaceous palaeogeographic evolution of the Coqen basin in the Lhasa Terrane, southern Tibetan plateau: Palaeogeography, Palaeoclimatology, Palaeoecology, v. 485, p. 101–118, https://doi.org/10.1016/j.palaeo.2017.06.006.

Sun, S.J., Sun, W.D., Zhang, L.P., Zhang, R.Q., Li, C.Y., Zhang, H., Hu, Y.B., and Zhang, Z.R., 2015b, Zircon U–Pb ages and geochemical characteristics of granitoids in Nagqu area, Tibet: Lithos, v. 231, p. 92–102, https://doi.org/10.1016/j.lithos.2015.06.003.

Sun, S.-s., and McDonough, W.F., 1989, Chemical and isotopic systematics of oceanic basalts: Implications for mantle composition and processes, *in* Saunders, A.D., and Norry, M.J., eds., Magmatism in the Ocean Basins: Geological Society, London, Special Publication 42, p. 313–345, https://doi.org/10.1144/GSL.SP.1989.042.01.19.

Tang, J., Zhang, Z., Allen, M.B., Song, S., Ding, C., Li, K., and Chen, Y., 2024, Origin of Early Cretaceous mafic volcanic rocks from the Erlian Basin west of the Great Xing'an Range of North China: Implications for the tectono-magmatic evolution of East Asia: Geological Society of America Bulletin, v. 136, p. 3085–3102, https://doi.org/10.1130/B37068.1.

Tang, M., Wang, X.L., Shu, X.J., Wang, D., Yang, T., and Gopon, P., 2014, Hafnium isotopic heterogeneity in zircons from granitic rocks: Geochemical evaluation and modeling of "zircon effect" in crustal anatexis: Earth and Planetary Science Letters, v. 389, p. 188–199, https://doi.org/10.1016/j.epsl.2013.12.036.

Thirlwall, M.F., Smith, T.E., Graham, A.M., Theodorou, N., Hollings, P., Davidson, J.P., and Arculus, R.J., 1994, High field strength element anomalies in arc lavas: Source or process?: Journal of Petrology, v. 35, p. 819–838, https://doi.org/10.1093/petrology/35.3.819.

Wang, J.G., Hu, X., Garzanti, E., An, W., and Liu, X.C., 2017, The birth of the Xigaze forearc basin in southern Tibet: Earth and Planetary Science Letters, v. 465, p. 38–47, https://doi.org/10.1016/j.epsl.2017.02.036.

Wang, J.G., Hu, X., Garzanti, E., BouDagher-Fadel, M.K., Liu, Z.C., Li, J., and Wu, F.Y., 2020, From extension to tectonic inversion: Mid-Cretaceous onset of Andean-type orogeny in the Lhasa block and early topographic growth of Tibet: Geological Society of America Bulletin, v. 132, p. 2432–2454, https://doi.org/10.1130/B35314.1.

Wang, L., Zeng, L.S., Gao, L.E., and Chen, Z.Y., 2013, Early Cretaceous high Mg-# and high Sr/Y clinopyroxene-bearing diorite in the southeast Gangdese batholith, Southern Tibet: Acta Petrologica Sinica (Yanshi Xuebao), v. 29, p. 1977–1994.

Wang, Q., Meng, Y., Wei, Y., Jiang, L., Wang, Z., and Mao, G., 2022, Identification of the Early Cretaceous granitic pluton and tectonic implications in the middle Gangdese belt, southern Tibet: Frontiers of Earth Science, v. 10, https://doi.org/10.3389/feart.2022.979313.

Wang, W., Zhai, Q.G., Hu, P.Y., Tang, Y., Wang, H.T., and Zhu, Z.C., 2023, Magmatic records of subduction and closure of the Meso-Tethys Ocean in the northern-central Tibetan Plateau: Geological Society of America Bulletin, v. 135, p. 2849–2867, https://doi.org/10.1130/B36593.1.

Wang, Y., Peate, I.U., Luo, Z., Wang, S., Cheng, L., Hao, J., and Wang, Y., 2019, Rifting in SW China: Structural and sedimentary investigation of the initial crustal response to emplacement of the Permian Emeishan LIP: Geological Magazine, v. 156, p. 745–758, https://doi.org/10.1017/S0016756818000171.

Wiedenbeck, M., Allé, P., Corfu, F.Y., Griffin, W.L., Meier, M., Oberli, F.V., Quadt, A.V., Roddick, J.C., and Spiegel, W., 1995, Three natural zircon standards for U-Th-Pb, Lu-Hf, trace element and REE analyses: Geostandards Newsletter, v. 19, p. 1–23, https://doi.org/10.1111/j.1751-908X.1995.tb00147.x.

Weis, D., Kieffer, B., Maerschalk, C., Barling, J., De Jong, J., Williams, G.A., Hanano, D., Pretorius, W., Mattielli, N., Scoates, J.S., Goolaert, A., Friedman, R.M., and Mahoney, J.B., 2006, High-precision isotopic characterization of USGS reference materials by TIMS and MC-ICP-MS: Geochemistry, Geophysics, Geosystems, v. 7, https://doi.org/10.1029/2006GC001283.

Wen, D.J., Hu, X., Yu, J.H., Wang, X.L., Chapman, T., and Wang, R.Q., 2023, Origin of Late Cretaceous, enclave-bearing granitoids in southern Tibet: Implications for magma recharge and crustal thickening: Geological Society of America Bulletin, v. 135, p. 2391–2406, https://doi.org/10.1130/B36530.1.

Wilson, M., ed., 1989, Igneous Petrogenesis: A Global Tectonic Approach: Dordrecht, Springer Netherlands, 466 p., https://doi.org/10.1007/978-1-4020-6788-4.

Xu, Y., Wang, Q., Tang, G., Wang, J., Li, H., Zhou, J., Li, Q.W., Qi, Y., Liu, P.P., Ma, L., and Fan, J., 2020, The origin of arc basalts: New advances and remaining questions: Science China Earth Sciences, v. 63, p. 1969–1991, https://doi.org/10.1007/s11430-020-9675-y.

Xu, Y., Hu, X., Garzanti, E., BouDagher-Fadel, M., Sun, G., Lai, W., and Zhang, S., 2022, Mid-Cretaceous thick carbonate accumulation in Northern Lhasa (Tibet): Eustatic vs. tectonic control?: Geological Society of America Bulletin, v. 134, p. 389–404, https://doi.org/10.1130/B35930.1.

Yang, J.H., Sun, J.F., Chen, F.K., Wilde, S.A., and Wu, F.Y., 2007, Sources and petrogenesis of Late Triassic dolerite dikes in the Liaodong Peninsula: Implications for post-collisional lithosphere thinning of the eastern North China Craton: Journal of Petrology, v. 48, p. 1973–1997, https://doi.org/10.1093/petrology/egm046.

Yin, A., and Harrison, T.M., 2000, Geologic evolution of the Himalayan-Tibetan orogen: Annual Review of Earth and Planetary Sciences, v. 28, p. 211–280, https://doi.org/10.1146/annurev.earth.28.1.211.

Yu, J.J., Chen, W., Tang, J.X., Wang, C.Y., Ma, X.D., Liu, Q.P., Di, M.X., and Liu, C., 2024, Petrogenesis of the Zenong Group volcanics in the central Lhasa subterrane, Tibet: Geodynamic implications of the scissor-like southward subduction of the Shiquanhe-Jiali Tethyan Ocean: Lithos, v. 490, https://doi.org/10.1016/j.lithos.2024.107831.

Zeng, Y.C., Xu, J.F., Chen, J.L., Wang, B.D., Kang, Z.Q., and Huang, F., 2018, Geochronological and geochemical constraints on the origin of the Yunzhug ophiolite in the Shiquanhe–Yunzhug–Namu Tso ophiolite belt, Lhasa Terrane, Tibetan Plateau: Lithos, v. 300, p. 250–260, https://doi.org/10.1016/j.lithos.2017.11.025.

Zhang, K.J., Xia, B.D., Wang, G.M., Li, Y.T., and Ye, H.F., 2004, Early Cretaceous stratigraphy, depositional environments, sandstone provenance, and tectonic setting of central Tibet, western China: Geological Society of America Bulletin, v. 116, p. 1202–1222, https://doi.org/10.1130/B25388.1.

Zhu, D.C., Mo, X.X., Niu, Y., Zhao, Z.D., Wang, L.Q., Liu, Y.S., and Wu, F.Y., 2009, Geochemical investigation of Early Cretaceous igneous rocks along an east–west traverse throughout the central Lhasa Terrane, Tibet: Chemical Geology, v. 268, p. 298–312, https://doi.org/10.1016/j.chemgeo.2009.09.008.

Zhu, D.C., Zhao, Z.D., Niu, Y., Mo, X.X., Chung, S.L., Hou, Z.Q., Wang, L.Q., and Wu, F.Y., 2011, The Lhasa Terrane: Record of a microcontinent and its histories of drift and growth: Earth and Planetary Science Letters, v. 301, p. 241–255, https://doi.org/10.1016/j.epsl.2010.11.005.

Zhu, D.C., Zhao, Z.D., Niu, Y., Dilek, Y., Wang, Q., Ji, W.H., Dong, G.C., Sui, Q.L., Liu, Y.S., Yuan, H.L., and Mo, X.X., 2012, Cambrian bimodal volcanism in the Lhasa Terrane, southern Tibet: Record of an early Paleozoic Andean-type magmatic arc in the Australian proto-Tethyan margin: Chemical Geology, v. 328, p. 290–308, https://doi.org/10.1016/j.chemgeo.2011.12.024.

Zhu, D.C., Zhao, Z.D., Niu, Y., Dilek, Y., Hou, Z.Q., and Mo, X.X., 2013, The origin and pre-Cenozoic evolution of the Tibetan Plateau: Gondwana Research, v. 23, p. 1429–1454, https://doi.org/10.1016/j.gr.2012.02.002.

Zhu, D.C., Li, S.M., Cawood, P.A., Wang, Q., Zhao, Z.D., Liu, S.A., and Wang, L.Q., 2016, Assembly of the Lhasa and Qiangtang terranes in central Tibet by divergent double subduction: Lithos, v. 245, p. 7–17, https://doi.org/10.1016/j.lithos.2015.06.023.

Zhu, D.C., Wang, Q., Weinberg, R.F., Cawood, P.A., Chung, S.L., Zheng, Y.F., Zhao, Z.D., Hou, Z.Q., and Mo, X.X., 2022, Interplay between oceanic subduction and continental collision in building continental crust: Nature Communications, v. 13, 7141, https://doi.org/10.1038/s41467-022-34826-0.

Zhu, D.C., Wang, Q., Weinberg, R.F., Cawood, P.A., Zhao, Z., Hou, Z.Q., and Mo, X.X., 2023, Continental crustal growth processes recorded in the Gangdese Batholith, southern Tibet: Annual Review of Earth and Planetary Sciences, v. 51, p. 155–188, https://doi.org/10.1146/annurev-earth-032320-110452.

Zong, K., Klemd, R., Yuan, Y., He, Z., Guo, J., Shi, X., Liu, Y.S., Hu, Z.C., and Zhang, Z., 2017, The assembly of Rodinia: The correlation of early Neoproterozoic (ca. 900 Ma) high-grade metamorphism and continental arc formation in the southern Beishan Orogen, southern Central Asian Orogenic Belt (CAOB): Precambrian Research, v. 290, p. 32–48, https://doi.org/10.1016/j.precamres.2016.12.010.

Science Editor: Mihai Ducea
Associate Editor: Fangyang Hu

Manuscript Received 21 October 2024
Revised Manuscript Received 17 December 2024
Manuscript Accepted 12 March 2025